

A DYNAMIC STUDY OF FRAGMENTATION AND ENERGY LOSS DURING HIGH VELOCITY IMPACT

Ralph Zee, Principal Investigator

Table of Content

ABSTRACT	1
INTRODUCTION	3
MOMENTUM AND ENERGY DISTRIBUTION IN THE DEBRIS CLOUD	5
Initial Idea	5
Momentum versus Energy	7
Development of Momentum Monitoring	7
Development of Energy Monitoring	46
CHARACTERIZATION OF ENERGY LOSS IN ADVANCED MATERIALS FOR SECONDARY PROTECTION	62

A DYNAMIC STUDY OF FRAGMENTATION AND ENERGY LOSS DURING HIGH VELOCITY IMPACT

Ralph Zee, Principal Investigator

ABSTRACT

Research conducted under this contract can be divided into two main areas: hypervelocity (in the range up to 7 km/s) and high velocity (less than 1 km/s). Work in the former was performed at NASA-Marshall Space Flight Center using the Light Gas Gun Facility. The lower velocity studies were conducted at Auburn University using the ballistic gun.

The emphasis of the project was on the hypervelocity phenomenon especially in the characterization of the debris cloud formed by the primary impact events. Special devices were made to determine the angular distributions of momentum and energy of the debris cloud as a function of impact conditions. After several iteration processes, it was decided to concentrate on the momentum effort. Prototype devices were designed, fabricated and tested. These devices were based on the conservation of momentum. Distributions of the debris cloud formed were measured by determining the amount of momentum transferred from the debris cloud to strategically placed pendulum measurement devices. The motion of the pendula was monitored using integrated opto-interrupters. Six pendula were placed at scattering angles ranging from 10° to 40°. The device was found to be very durable even in the hostile environment that existed in the target chamber. An automated data acquisition system was used for data collection. Experimental findings were in accord with calculations. The distribution of the momentum in the debris cloud was found to be a strong function of the

impact condition. Small projectiles at high velocities were observed to produce finely dispersed debris whereas large projectiles generated discrete particles in the debris. Results also show that the momentum in the forward direction was enhanced due to the impact. This phenomenon of momentum multiplication was also observed in other studies and in computer simulations. It was initially planned to determine the energy distribution using deformation energy in a rod with strain gauges. Results from preliminary studies show that this technique is acceptable but too tedious. A new technique was explored based on measuring the heating effect of the debris cloud using an IR camera. The feasibility and sensitivity was established at Auburn University. This type of energy distribution measurement method can easily be adapted to the gas gun facility at MSFC.

The objective of the lower velocity studies at Auburn was to simulate the damage produced in advanced materials by the lower energy debris cloud. Graphite, Kevlar and PE reinforced composites. Results show that PE based materials possess the best impact resistance.

INTRODUCTION

The Space Station Freedom will be exposed to a hostile environment over long periods of time. Such long term exposure of systems in space may lead to degradation of materials as a direct result of their interactions with environmental factors. These factors include ultraviolet radiation, atomic oxygen, and hypervelocity particles. With the ever increasing amount of man-made debris, hyper-velocity impacts have become a critical concern of designers. Due to the high energies involved in these particle collisions, it is impossible to protect the space station using a single containment of weight limitations. One solution proposed by Whipple comprises of a system of plates which serve to intercept any incoming particle and render it harmless to the pressure wall. This is believed to occur by disintegrating the particle and redistributing its momentum over a large angle thus reducing its penetrating power. It is therefore necessary to design the bumper in such a manner as to maximize its effectiveness.

Earlier attempts designed to determine the effectiveness of proposed bumper materials relied solely upon examinations of witness plates which received the debris cloud after the initial impact occurred. Measurements of crater size and areal density were taken and recorded for future comparison with other testing conditions. This method, however, does not provide empirical data by which the designer can evaluate the effectiveness of the bumper for redistributing momentum. Up to the present time, several attempts have been made to measure the momentum of the ejecta produced from the collision between the projectile and the bumper. This was accomplished through the use of a ballistic pendulum system. Such systems are designed to measure the total momentum produced by such an impact by catching all of the

ejecta simultaneously. Unlike these previous attempts, the system devised in this experiment is capable of measuring the momentum of the debris at direct locations within the ejecta cloud. This results in the ability to characterize momentum more thoroughly than previously possible. Momentum profiles were obtained for a series of test conditions. In addition to providing a method for obtaining momentum distributions, the data obtained from this experiment will help to confirm whether or not an amplification of momentum occurs. This is necessary in determining the role played by the bumper in providing protection for the space vehicle. Total momentum values in the debris cloud were calculated from the debris momentum profiles. These results indicated that a momentum amplification exists with a multiplication factor of between 2 and 3. Thus the role of the bumper to serve as a means for momentum redistribution and not reduction was verified.

The main objective of this research project is to develop devices and techniques which are capable of determining the momentum and energy distributions in the debris cloud generated by the initial impact between the hypervelocity projectile and the bumper plate. Since the bumper does not completely absorb the energy of the primary impact, but rather distribute it, damage to the pressure wall from the debris cloud also needs to be examined. The second goal of the research is to determine the effects of the debris cloud on potential pressure wall materials.

MOMENTUM AND ENERGY DISTRIBUTION IN THE DEBRIS CLOUD

Initial Idea

In the initial proposal, a momentum sensing device was proposed to uniquely identify the mass and velocity distributions of the debris as a function of impact parameters and scattering angle. To determine the momentum distribution, a recoil device were to be used. The concept proposed was based on the conservation of linear momentum during impact. The experiment setup proposed was similar to that given in figure 1. The initial hypervelocity projectile (A) with mass M_1 and velocity V_1 will impact on the bumper material (B). Small fragments (masses m_i and speeds v_i) produced will exit the back face in the direction θ_i . A stopper recoil plate (C) made of aluminum of mass M_2 (must be a soft material so that energy and momentum can be easily absorbed) will be placed on a low friction cart. Due to the impact of the small fragments, the stopper sheet will recoil with a velocity V_2 . The total linear momentum of all the small fragments in the undeflected direction can then be obtained. Mathematically, this can be represented by

$$M_2 V_2 = \sum_i (m_i v_i \cos \theta_i) \quad [1]$$

This overall information is insufficient to uniquely clarify the velocity distribution of the debris. To accomplish that, a movable aperture (D) were to be inserted in between the bumper material (B) and the recoil stopper plate (C). This is shown schematically in figure 2. The aperture and the movable recoil plate assembly were to be mounted on a track pivoted about the point of impact. The aperture (D) will then isolate the debris scattered into θ_i for collision with the recoil plate. By systematically moving the aperture and the recoil plate assembly to different positions, the overall velocity of the debris in different θ_i angles will be determined. Mathematically, this

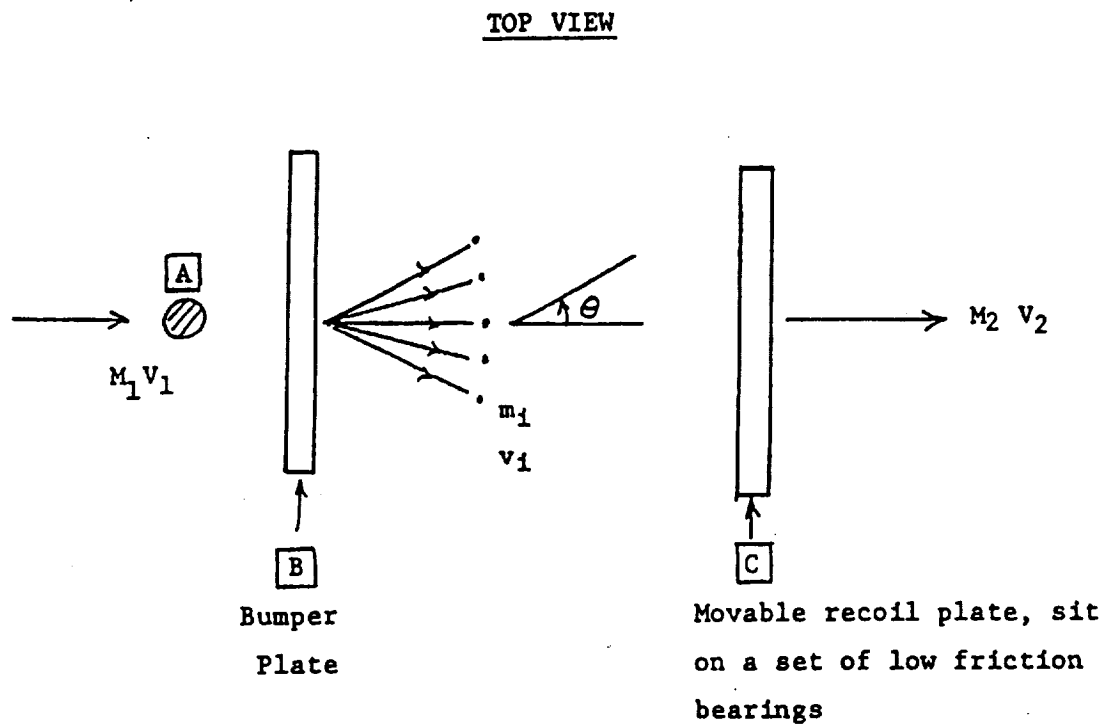


Figure 1. Basic experimental assembly for measuring momentum transfer from the debris cloud.

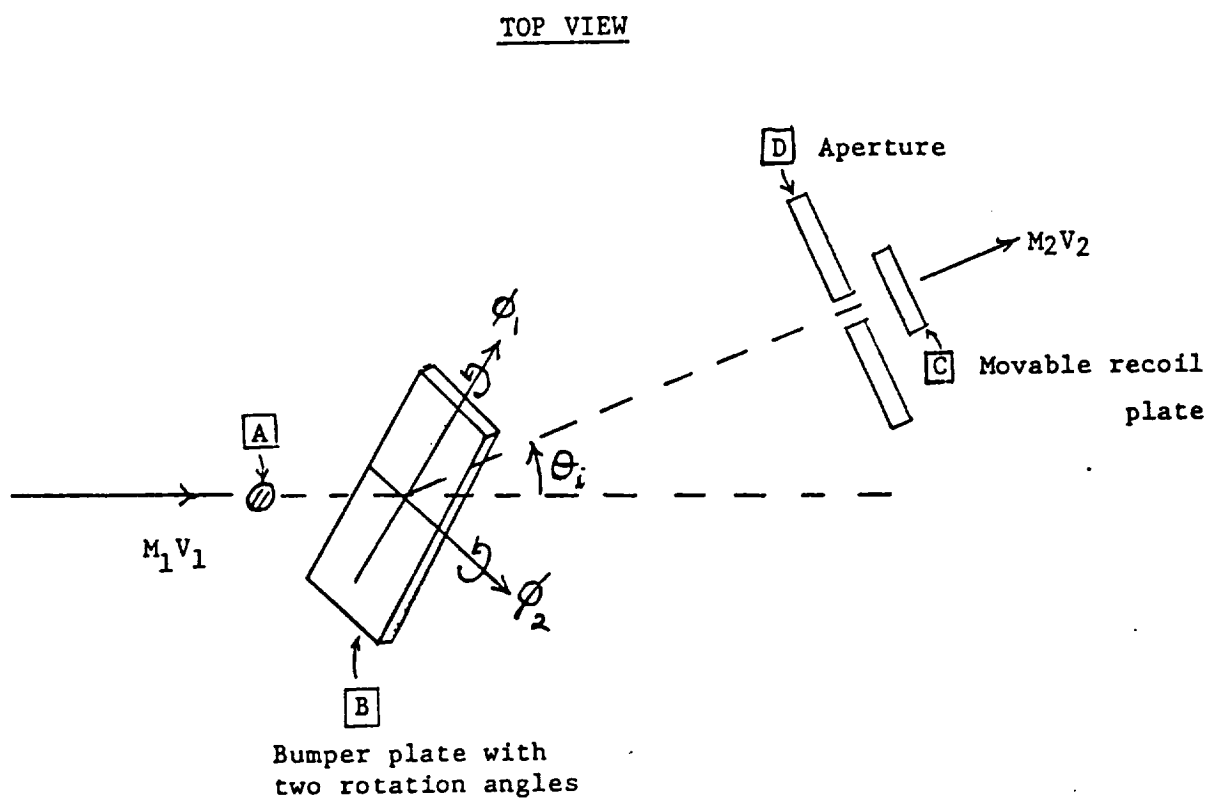


Figure 2. Experimental assembly with defining aperture. The schematic shown is for the more general non-normal incident configuration. In this research, effort was concentrated on normal incident.

condition can be represented by

$$M_2 V_2 = n_1 m_1 v_1 \quad [2]$$

where n_1 is the number of fragments of mass m_1 that pass through the aperture at angle θ_1 . Equation [2] does not contain the term $\cos \theta_1$ since all the selected debris passing through the aperture will impact the recoil plate at normal incidence. We assume that all the debris scattered into this aperture are uniform in size, which is acceptable if the aperture is small.

Preliminary calculations were performed to predict the parameters needed for this recoil system. As an estimation, we can assume that the hypervelocity projectile weighs 100 mg and has an initial velocity of 5 km/s. Furthermore, it is reasonable to assume that during the initial impact of the projectile with the bumper, only half of the initial momentum is available to set the recoil plate in motion. Of this total available momentum, only 1% is allowed to pass through the aperture. If the recoil plate has a mass of 100 gm, the resulting speed of this plate will be 2.5 cm/s which can be easily monitored using a series of relays at regular intervals.

To isolate the mass and velocity contributions to the momentum, the mass distribution of the debris as a function of scattered angle was to be determined by placing a heavy shield behind the bumper plate to stop the debris. These fragments will make indentions on the plate and the size of these indentions will provide the necessary mass distribution profile. This distribution is of course expected to be spherically symmetric and depends only on the scattered angle and the initial impact conditions.

Momentum versus Energy

However earlier in the project, it was determined that such a linear motion device is unacceptable due to the confined nature of the target chamber in the hypervelocity gun at MSFC. At that time a decision was made to determine both the energy and the momentum distributions in the debris cloud as a function of scattering angle θ . This is because such dual measurements would facilitate a direct and precise determination of both the mass and velocity without having to identify the mass directly since

$$v = \sqrt{(2E/p)} \quad [3]$$

and

$$m = p/v \quad [4]$$

A careful review of collision physics showed that in order to determine momentum transfer, the device must be able to response by a physical recoil motion whereas a energy measurement device would not have such a restriction.

Development for Momentum Monitoring

The objectives of this experiment are three-fold. The first objective is to design, construct, and test at device by which the momentum distribution could be monitored during a hypervelocity impact event. This requires that any equipment which resides in the test chamber be sufficiently durable to allow multiple uses without a substantial degradation in its capabilities. The second objective is to obtain momentum profiles for a set of test conditions. The final objective is to calculate the total momentum produced and verify the estimated amplification value.

The linear motion device proposed in the initial proposal was quickly replaced by a pendulum concept. Momentum transferred to the pendulum results

in the motion of the pendulum. Unfortunately, the period of the pendulum is independent of the impacted momentum. This means that it is necessary to monitor the real time motion of the pendulum instead of simply measuring its period. One approach will be to measure the velocity of the pendulum using two sensors at a fixed interval. After a careful study, we have adopted the basic design which requires only one optical sensor with one mechanical microswitch. The mechanical microswitch is for triggering. A series of periodic slots will be machined at the bottom of the pendulum which during the movement of the pendulum would introduce the required information in the optical sensor. A fast-response optical sensor such as Motorola H21 series slotted couplers/interrupter modules (response time in the microsecond range) will be ideal for this application. It is important to emphasize that both the duration of each cycle as well as time between cycles can be used to determine the momentum imparted on the pendulum. An aperture/shield assembly will be used in front of the pendulum to defined the scattering angle desired as well as to protect the pendulum system from debris damage. This basic design was improved during the course of the study and evolved into the final device. Figure 3 shows the actual signal stored on a digital oscilloscope from the motion of the pendulum.

The momentum measurement device was tested in the light gas gun facility (LGG) located at the Marshall Space Flight Center. The layout of this facility is shown in figure 4. The gun was used to propel spheres of various materials and sizes at velocities ranging from 5.0 to 7.5 km/sec at the targets. In this study aluminum (1100 Al) spheres were used as projectile and the bumper plates were comprised of 6061-T6 Al sheet. The momentum monitoring device was placed in the secondary test chamber. The bumper plate was places

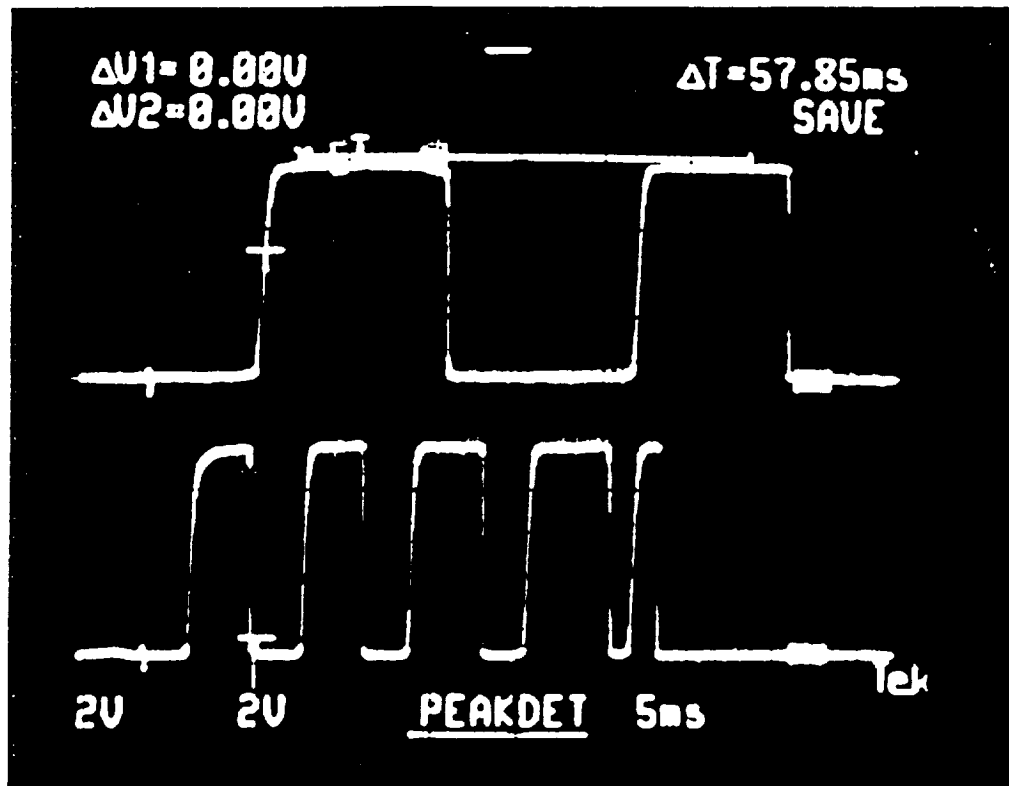


Figure 3. Discrete signal from the momentum device from which motion of the pendulum induced by the debris can be quantified for momentum determination.

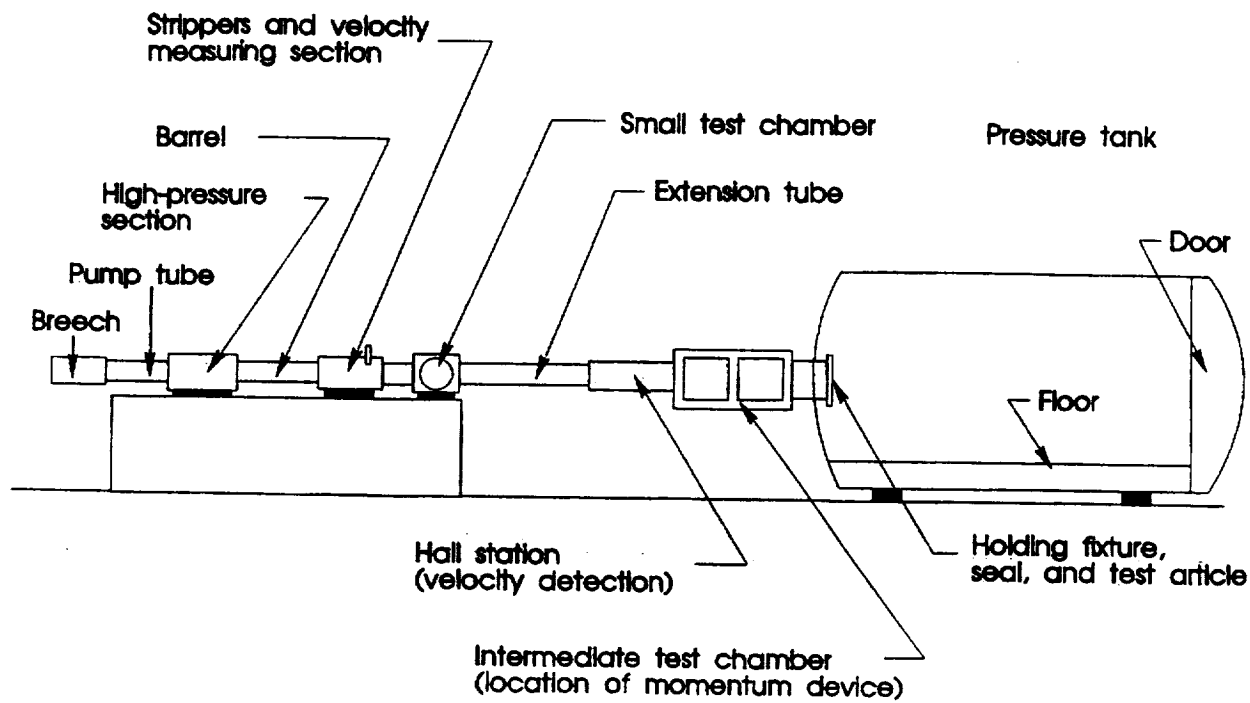


Figure 4. Layout of the light gas gun facility at NASA-MSFC.

at a distance of 15.24 cm (6") from the front of the blast shield protecting the device. During the tests, the chamber was evacuated to a vacuum of less than 300 millitorr. The primary impact between the aluminum projectile and the bumper produced a high energy debris cloud, the distribution of which is the center of investigation for this study.

The concept employed for this device involves the transfer of momentum from the incident ejects produced by the particle and bumper collisions onto pendula placed at periodic locations along a horizontal plane bisecting the debris cloud. A total of six pendula were employed at intervals of 10° beginning with 10° from the normal incident toward one side ending at 30° and beginning with 15° from normal incident ending at 35° on the other side. Figure 5 shows the typical configuration of the pendulum system while figure 6 shows the layout of all six pendulum system with respect to the bumper and incident particle. The mild steel blast protector serves to shield the pendula and other fragile components from the debris and gas surge while allowing a predetermined area of the pendulum impact block to be struck by incoming ejects. The pendula assemblies consist of an aluminum pendulum bar, impact block, and timing blade. The velocity of each pendulum is determined by the movement of the timing blade through an infrared photo-interrupter diode. Holes placed at regular intervals along the bottom edge of the timing blade serve to intermittently block and expose the beam produced by the infrared emitter located on one side of the diode allowing it to reach the sensor located on the opposite side of the blade. This results in a square wave potential drop alternating between 0 and 5 volts. Figure 7 illustrates a set of signals produced by all six pendulums simultaneously during an impact event.

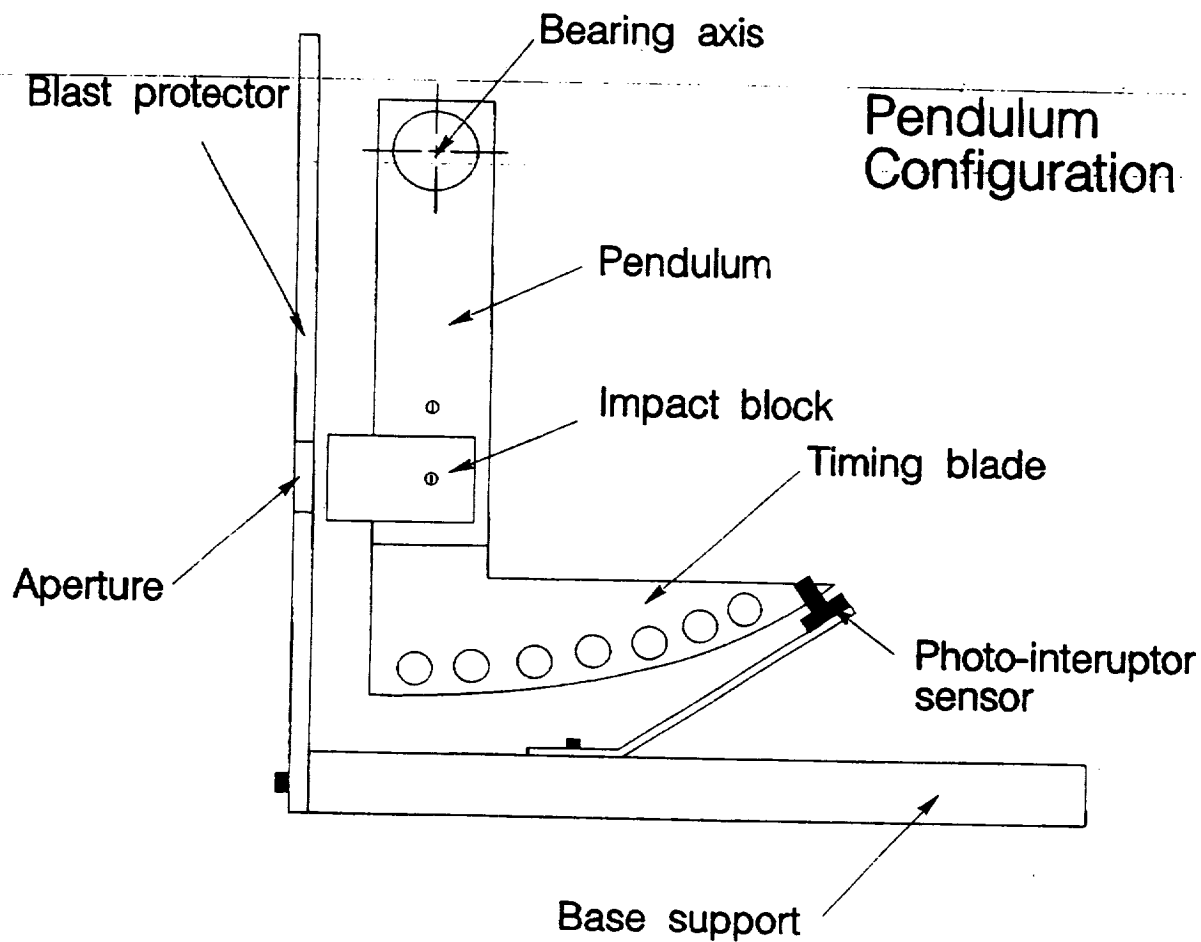


Figure 5. Basic pendulum configuration for momentum measurement.

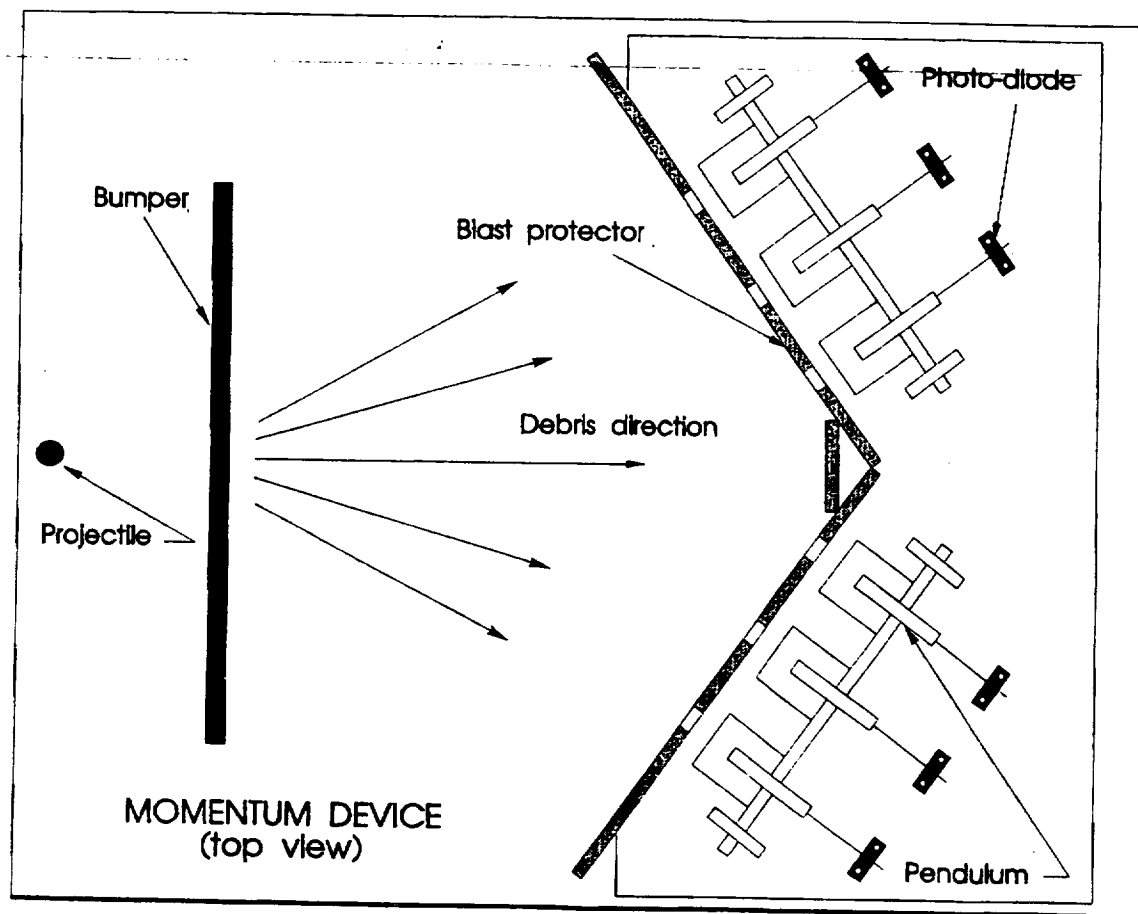


Figure 6. Arrangement of the pendula on the momentum measurement device.

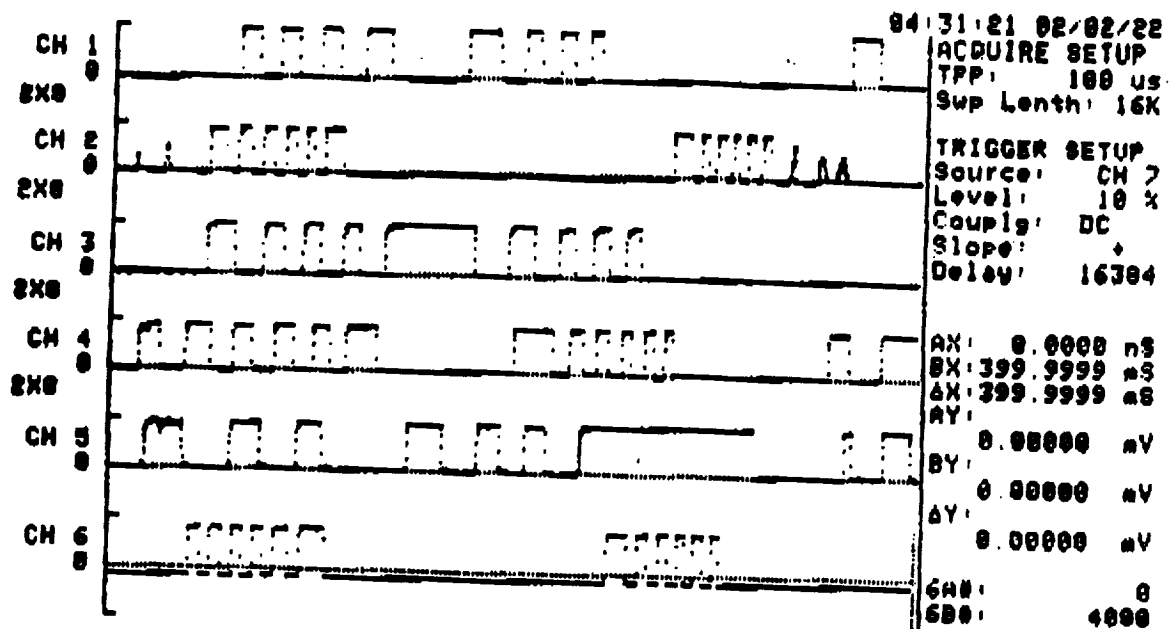


Figure 7. Signals produced by the opto-interrupters during impact. These data are stored on the Norland system.

Data collection and storage is accomplished through the use of a digital storage oscilloscope. Initial development of the device required four channels for data acquisition with triggering performed manually. This was accomplished through the use of two Tektronix storage oscilloscopes. The device used in this study requires six channels, one for each pendulum, and one channel for remote triggering. The data is recorded on a ten channel Norland A200i digital oscilloscope and saved on floppy diskettes for further analysis. Triggering is accomplished by imputing a signal produced by an x-ray flash detector used in determining projectile velocity into an unused channel. Total time duration for data acquisition is about 2 seconds which sufficiently allows for all the pendulums to pass through their upward and downward arcs at least one.

The device worked well for more than 40 shots with no significant reduction in sensitivity. Only a small amount of adjustment every 4 to 5 shots was required to tighten any loose bolts and replace damaged blast shields. After approximately 10 shots the device was removed and examined for any damage to electronic or structural components and cleaned. The diodes were replaced after approximately 25 shots and the pendulum impact blocks were replaced after every 15 shots.

The momentum monitoring device basically monitors the angular movement of each pendulum induced by the ejects from the impact. This motion is directly related to the momentum transfer from the specific portion of the cloud to the respective pendulum. It is therefore necessary to determine the conversion factor from the angular velocity to momentum density P' . The momentum from the debris cloud (mv) must equal the angular momentum induced in the pendulum as stated below in equation [5]. It is important to note here

the distinction of this momentum value with the particle momentum ($m_0 v_0$),

$$mv = I\omega/r \quad [5]$$

where $\omega = v/R$ [6]

Substitution of equation [6] into equation [5] yields the following which correlates the momentum (P) with the incident debris velocity (v)

$$P = Iv/rR \quad [7]$$

where $P = mv$ (debris momentum)

R = radius of arc traced by the timing blade

v = velocity of the timing blade

r = distance from center of axle to center of gravity

I = moment of inertia for the pendulum

In this study, $R=5.13"$, $r=3.5"$ and $I=4285 \text{ gm-cm}^2$. Substitution of these values into equation [7] gives

$$P \text{ (kg-cm/s)} = A \cdot v \quad [8]$$

where $A = 0.038$ [9]

Therefore, multiplication of the measured velocity, v , by the computed constant, A , gives the desired momentum values. This parameter A is a function of the inertias of the pendulum which was experimentally determined. To obtain the momentum per unit area P' , the values determined in the previous step are divided by the area of the apertures in the blast protector of the area of the impact block exposed to the debris.

Using the previously described method and equations [8] and [9], it is then possible to calculate the momentum values from the velocities obtained for each pendulum. More than forty shots were made using the design. Twenty two of these shots yielded useful information on the momentum distribution in the debris cloud. The conditions of the shots can be divided into four

categories: Group A: small projectile (0.25" diameter) and thin bumper (0.04" thick), Group B: small projectile and thick bumper (0.08" thick), Group C: large projectile (0.313" diameter) and thin bumper, Group D: large projectile and thick bumper. Table 1 summarizes the conditions for the tests conducted in this study. These distributions are shown in figures 8 to 30. It is evident from the profiles shown in these figures that the debris clouds formed by the impact of small projectiles (0.25" diameter, Groups A and B) have momentum concentrated in the middle and decay with scattering angle. However the momentum distributions in the debris generated by the larger projectiles (Groups C and D) are more discrete and spread out to large scattering angles. In some cases (such as Z-54) the pendula at large scattering angles actually received more momenta than the undeflected direction. This indicate that discrete fragments were formed under this impact condition.

The profiles from the impact of small projectiles can be fitted with either a Gaussian or triangular shape within the limit of experimental accuracy. However, the expected symmetry in these profiles is not always evident. This is due in part to variations present in the LGG system with respect to its ability to direct the projectile at the center of the bumper plate. Thus, the peak values can and are often observed toward one side of the center position or the other.

It appears that within the experimental scatters of the data, it is appropriate to fit the momentum distribution to either a Gaussian or triangular shape. The latter was selected to fit the data due to simplicity. Such a distribution can be characterized by two parameters: peak value of the momentum areal density P' and half width (radius r_0) at he bass. Total momentum in the debris cloud (P_{tot}) was then calculated from these values by

Z-26
0.25" Projectile
5 km/s
0.04" Bumper

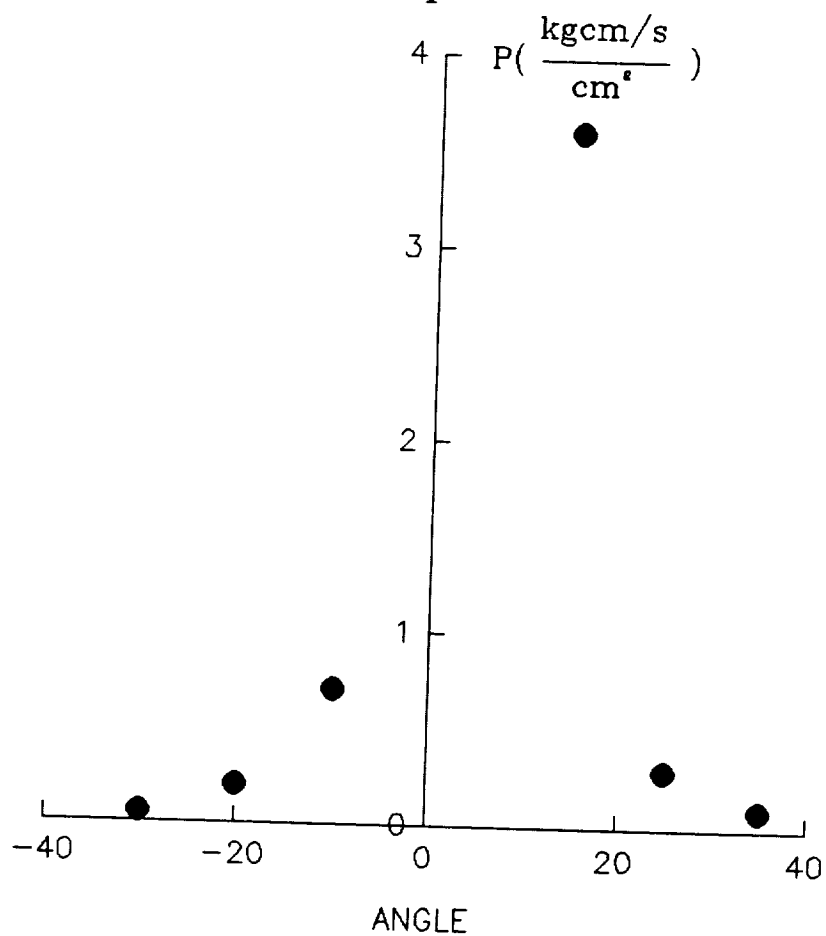


Figure 8. Momentum distribution obtained using the momentum device.

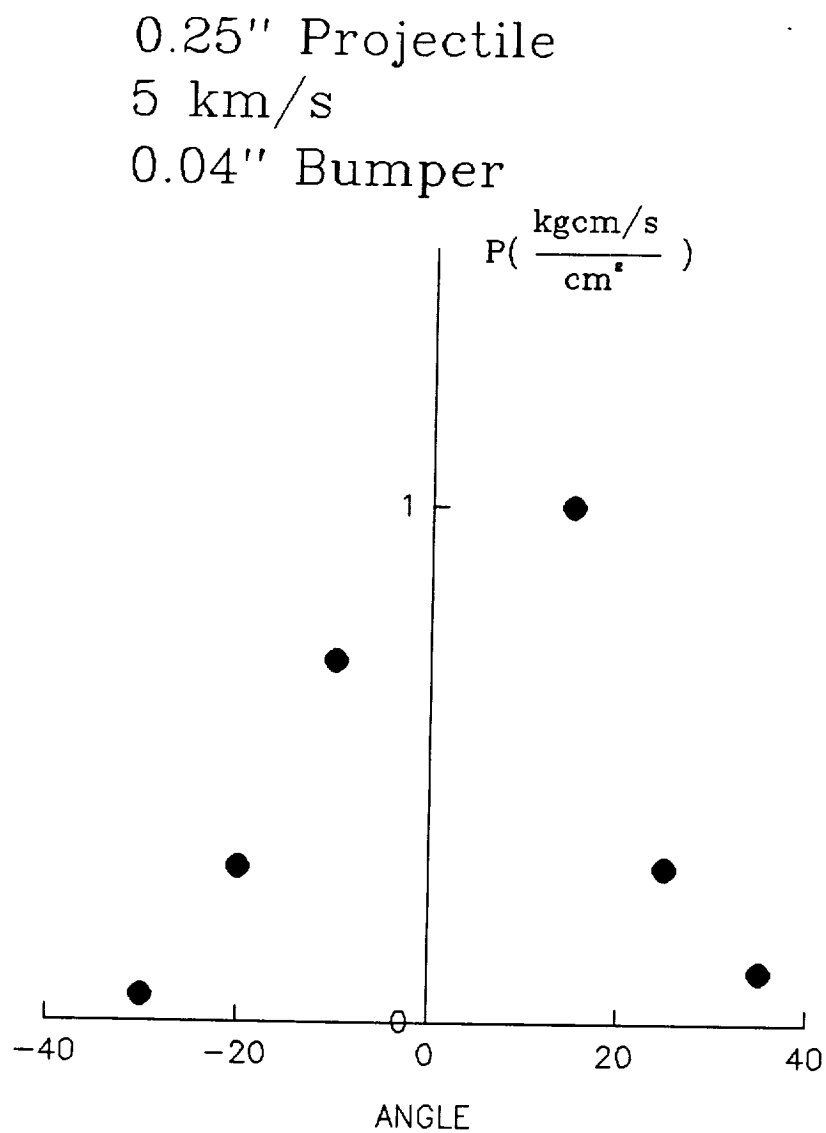


Figure 9. Momentum distribution obtained using the momentum device.

Z-50
0.25" Projectile
6 km/s
0.04" Bumper

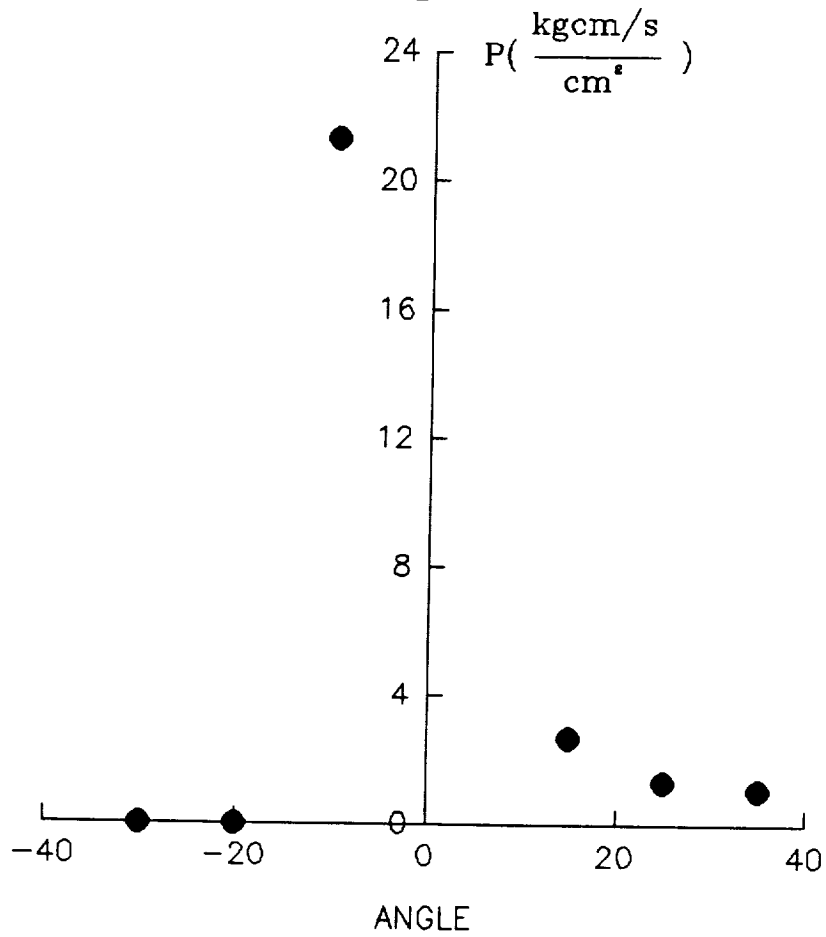


Figure 10. Momentum distribution obtained using the momentum device.

Z-24
0.25" Projectile
6 km/s
0.05" Bumper

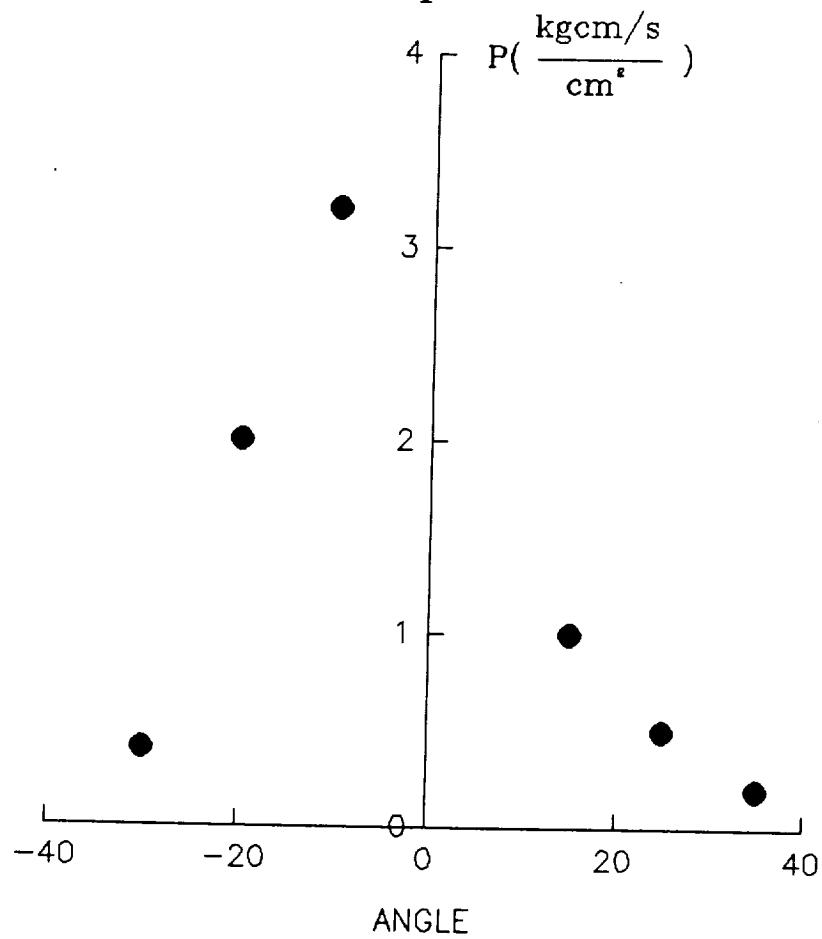


Figure 11. Momentum distribution obtained using the momentum device.

Z-47
0.25" Projectile
6 km/s
0.05" Bumper

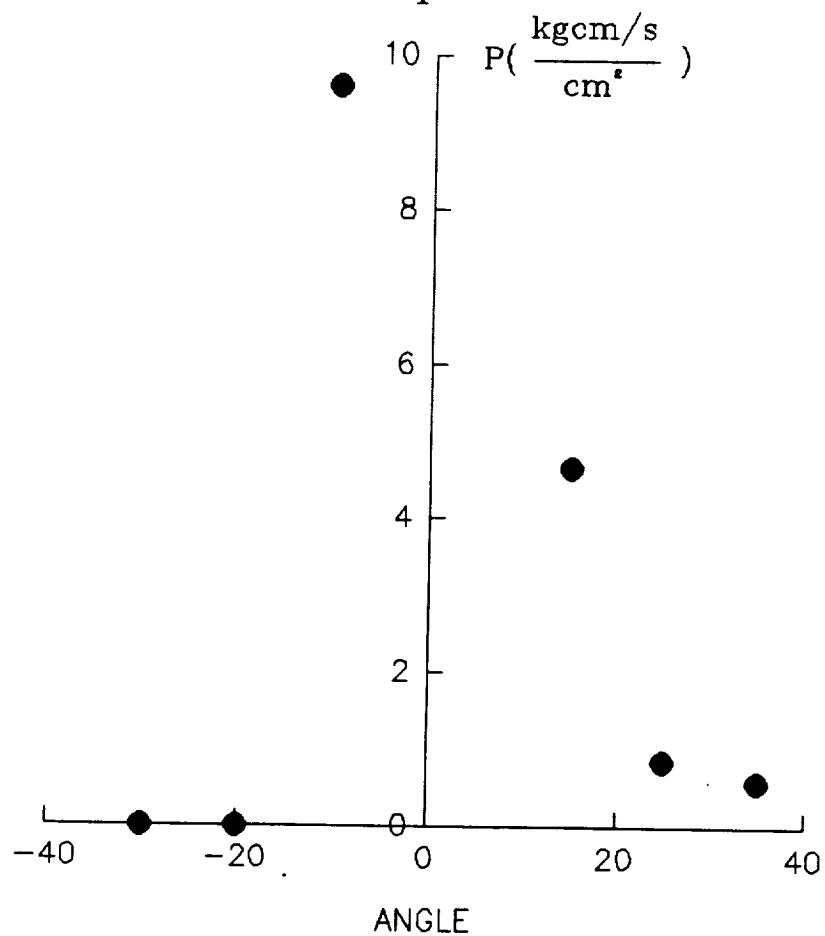


Figure 12. Momentum distribution obtained using the momentum device.

Z-31
0.25" Projectile
7.2 km/s
0.04" Bumper

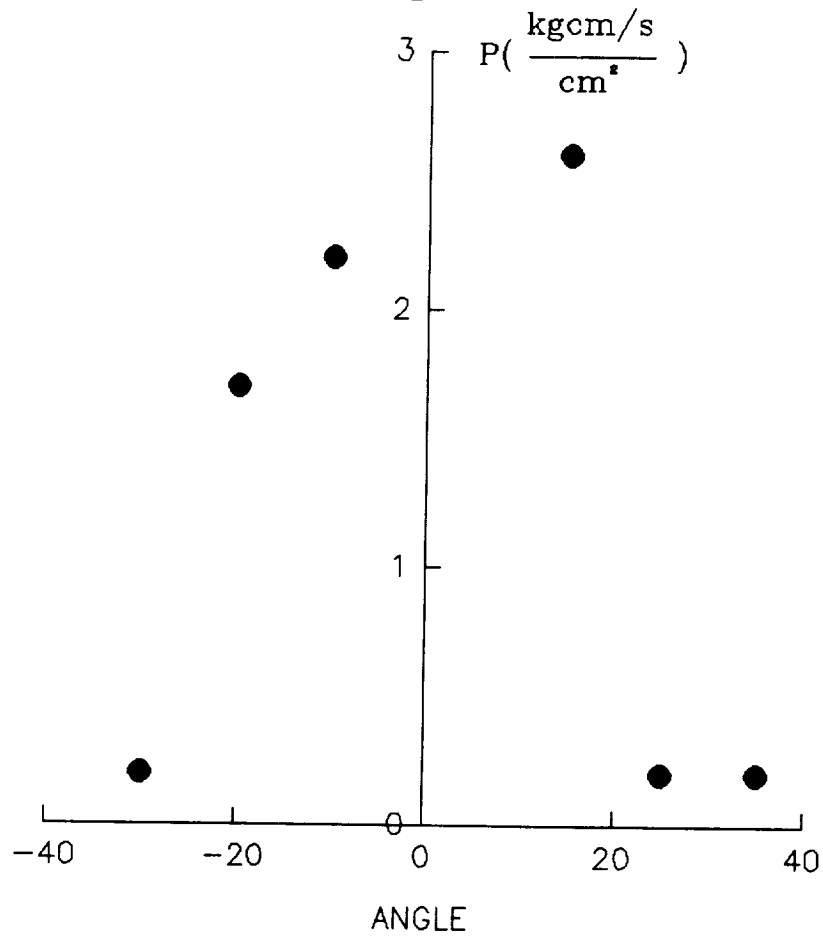


Figure 13. Momentum distribution obtained using the momentum device.

Z-38
0.25" Projectile
7.2 km/s
0.04" Bumper

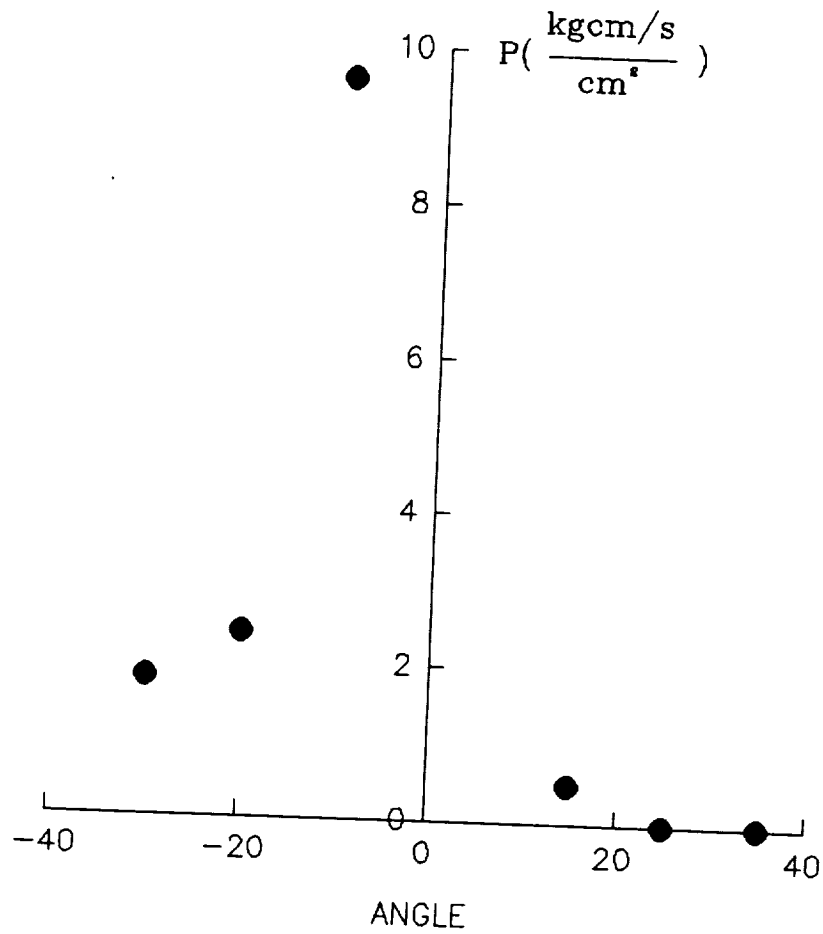


Figure 14. Momentum distribution obtained using the momentum device.

0.25" Projectile
5 km/s
0.08" Bumper

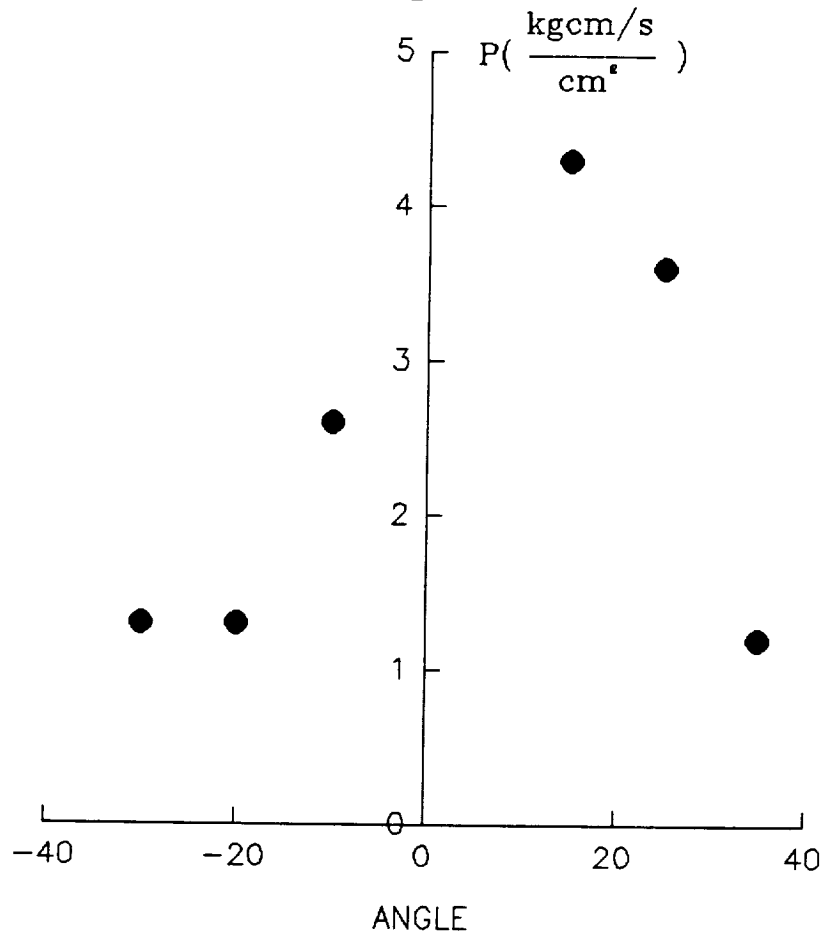


Figure 15. Momentum distribution obtained using the momentum device.

Z-39
0.25" Projectile
6 km/s
0.08" Bumper

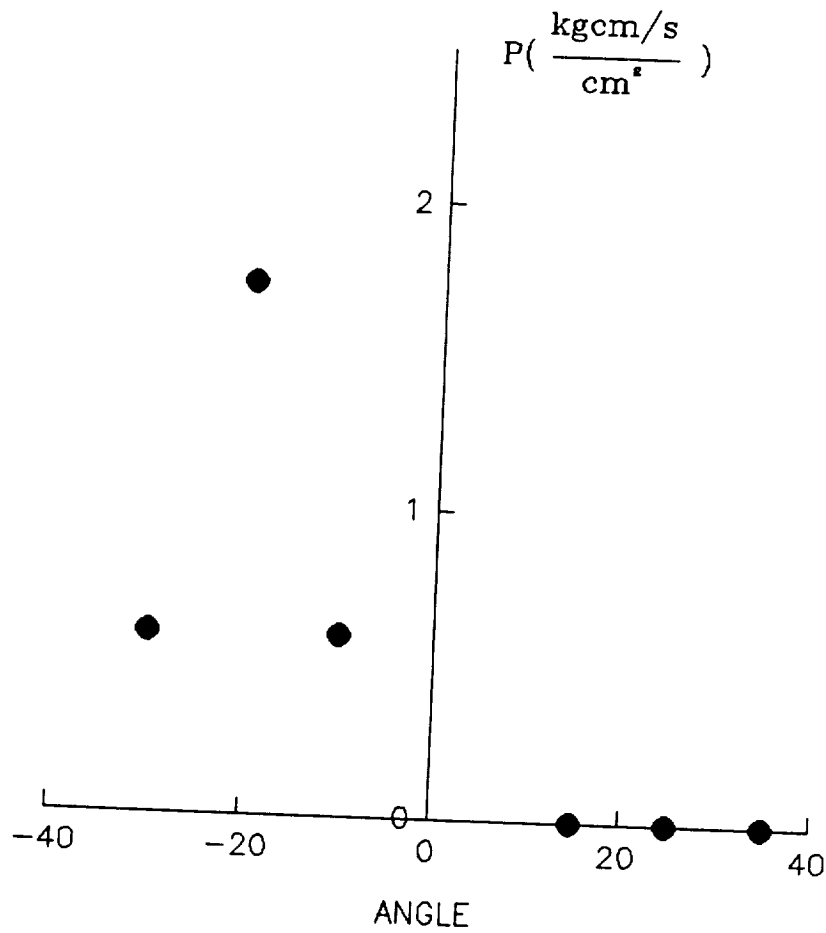


Figure 16. Momentum distribution obtained using the momentum device.

Z-48
0.25" Projectile
6 km/s
0.08" Bumper

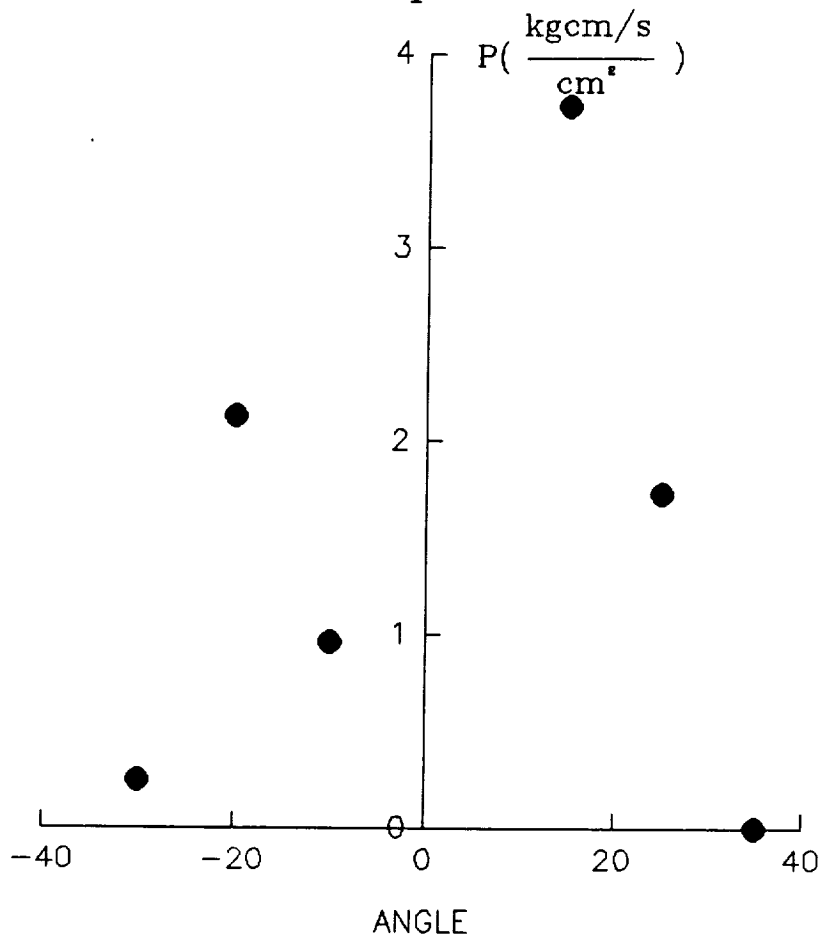


Figure 17. Momentum distribution obtained using the momentum device.

Z-51
0.25" Projectile
6 km/s
0.08" Bumper

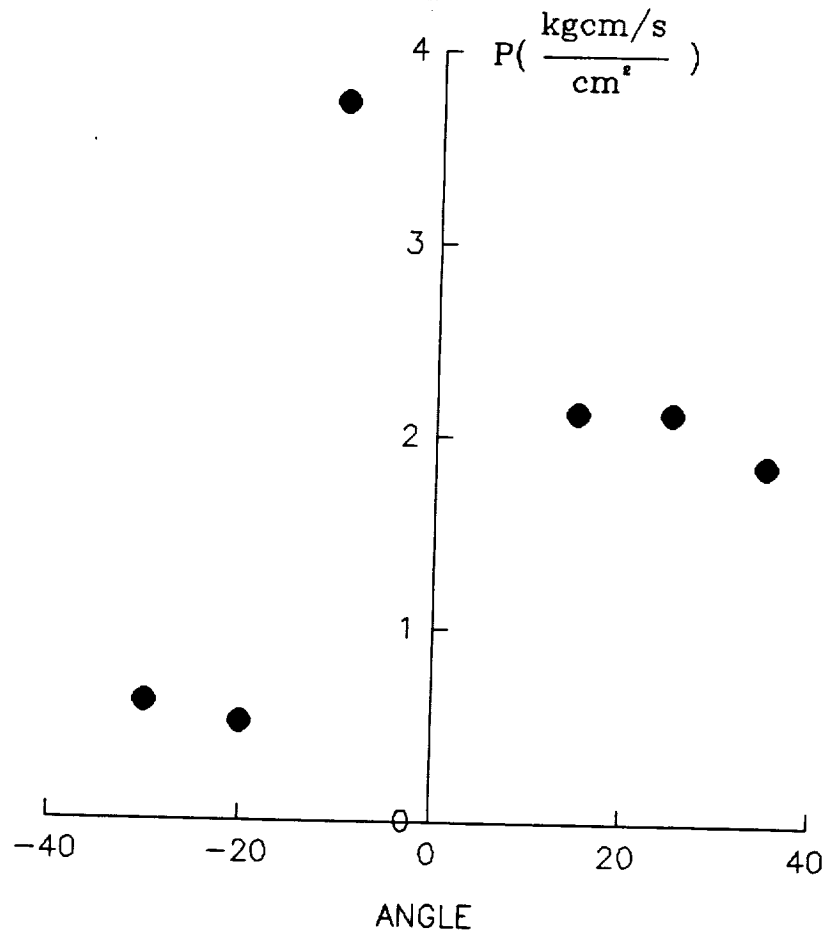


Figure 18. Momentum distribution obtained using the momentum device.

0.25" Projectile
6.5 km/s
0.08" Bumper

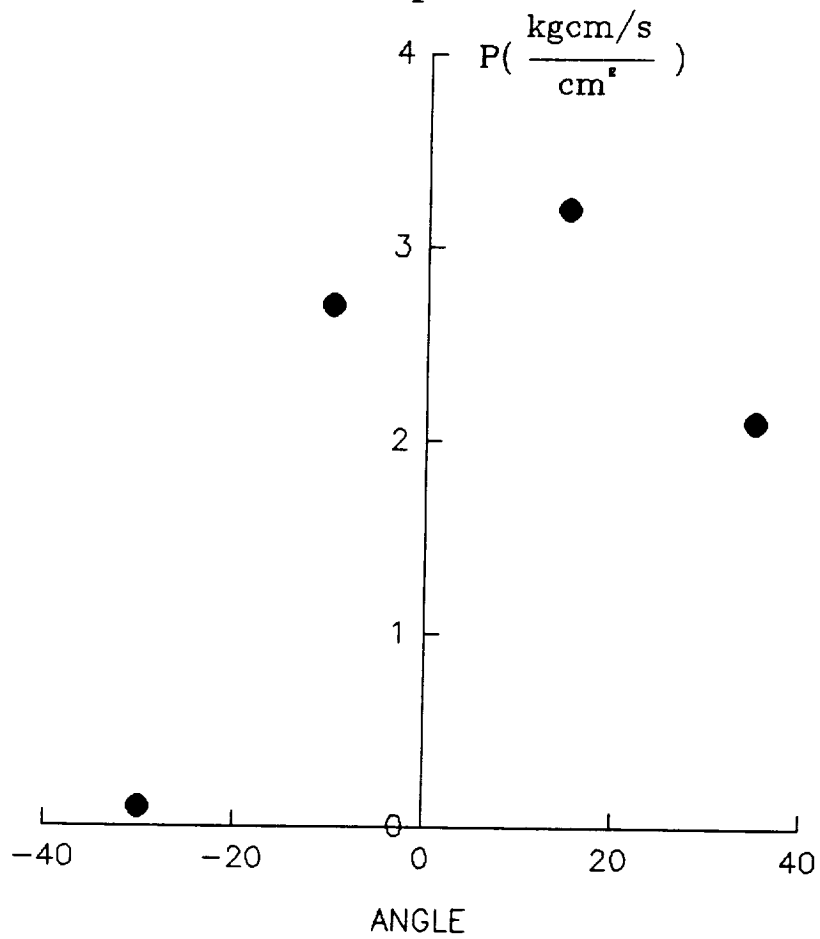


Figure 19. Momentum distribution obtained using the momentum device.

0.25" Projectile
7 km/s
0.08" Bumper

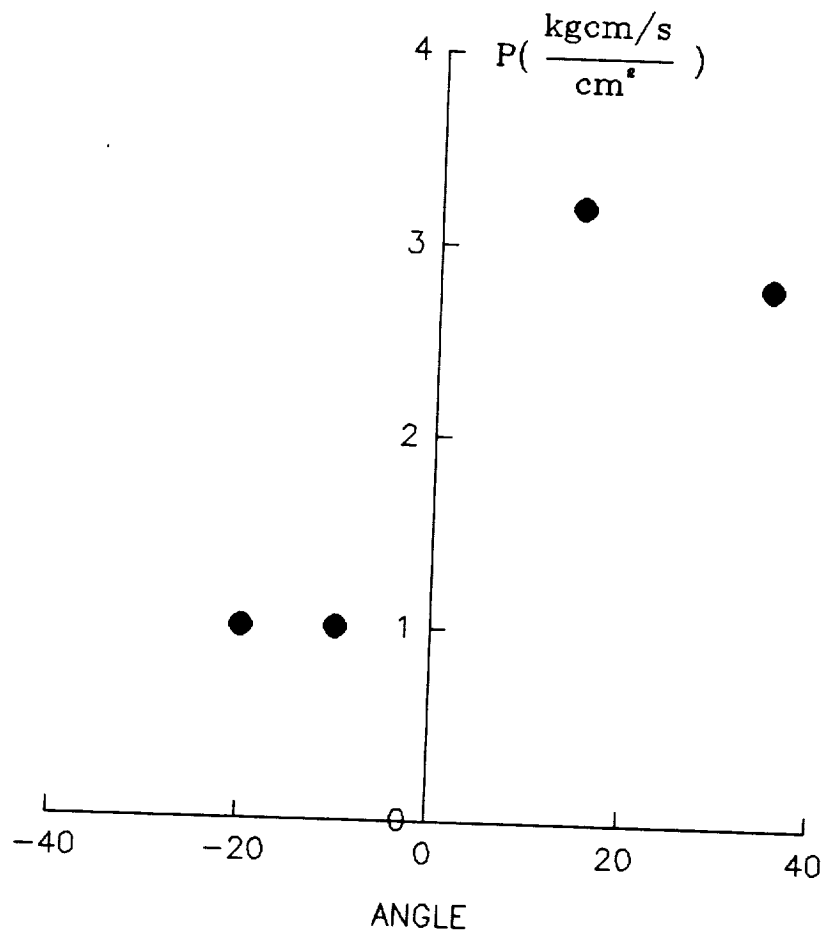


Figure 20. Momentum distribution obtained using the momentum device.

Z-33
0.25" Projectile
7.2 km/s
0.08" Bumper

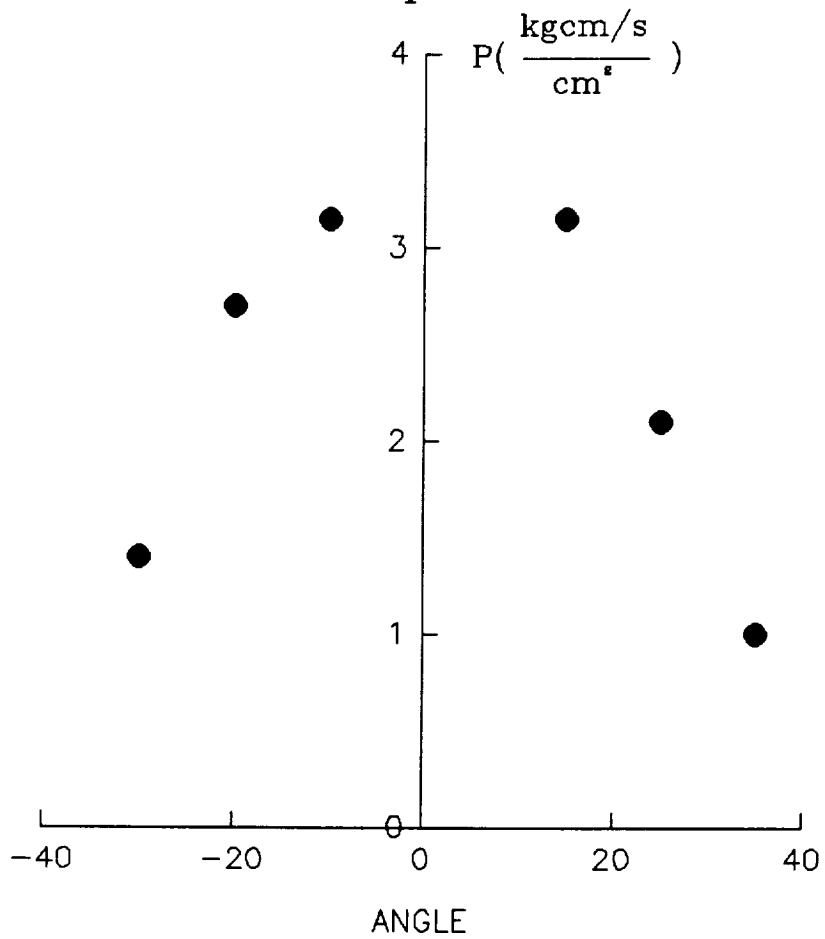


Figure 21. Momentum distribution obtained using the momentum device.

Z-32
0.25" Projectile
7.2 km/s
0.08" Bumper

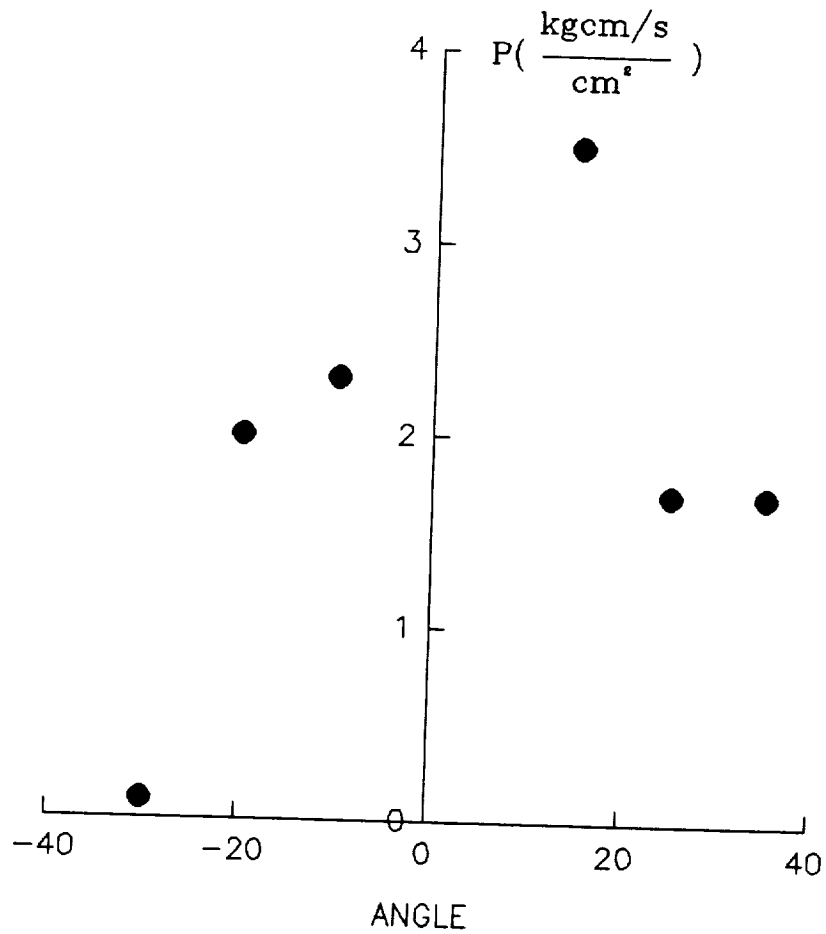


Figure 22. Momentum distribution obtained using the momentum device.

0.313" Projectile

6 km/s

0.04" Bumper

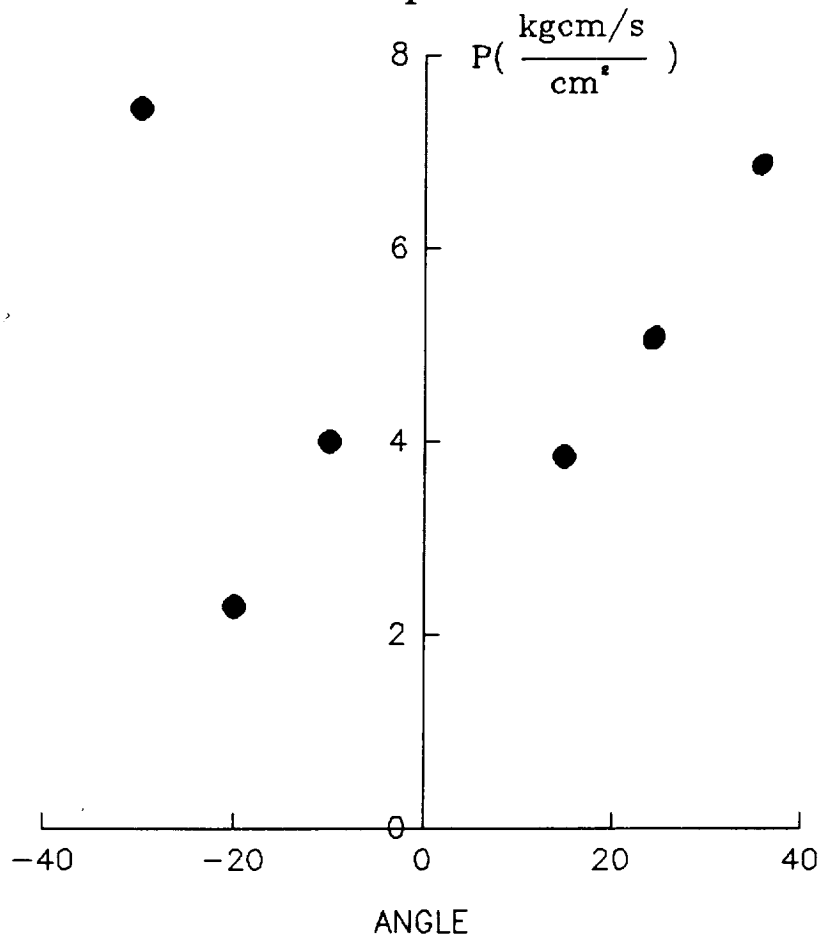


Figure 23. Momentum distribution obtained using the momentum device.

Z-44
0.313" Projectile
6 km/s
0.04" Bumper

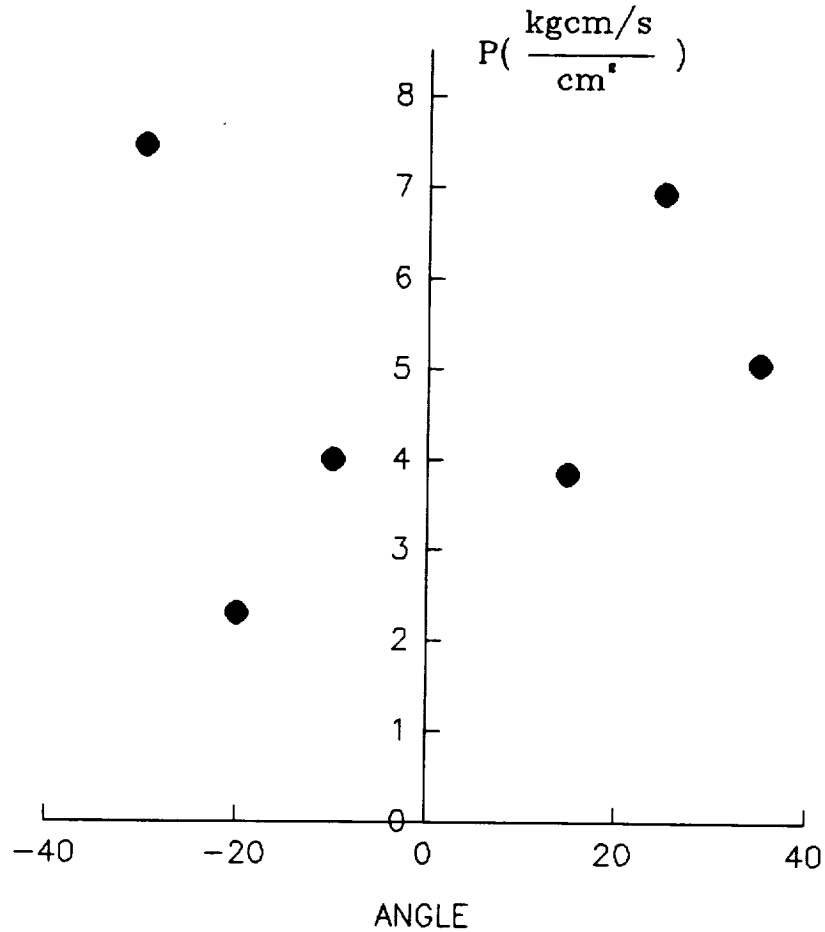


Figure 24. Momentum distribution obtained using the momentum device.

Z-56
0.313" Projectile
7.2 km/s
0.04" Bumper

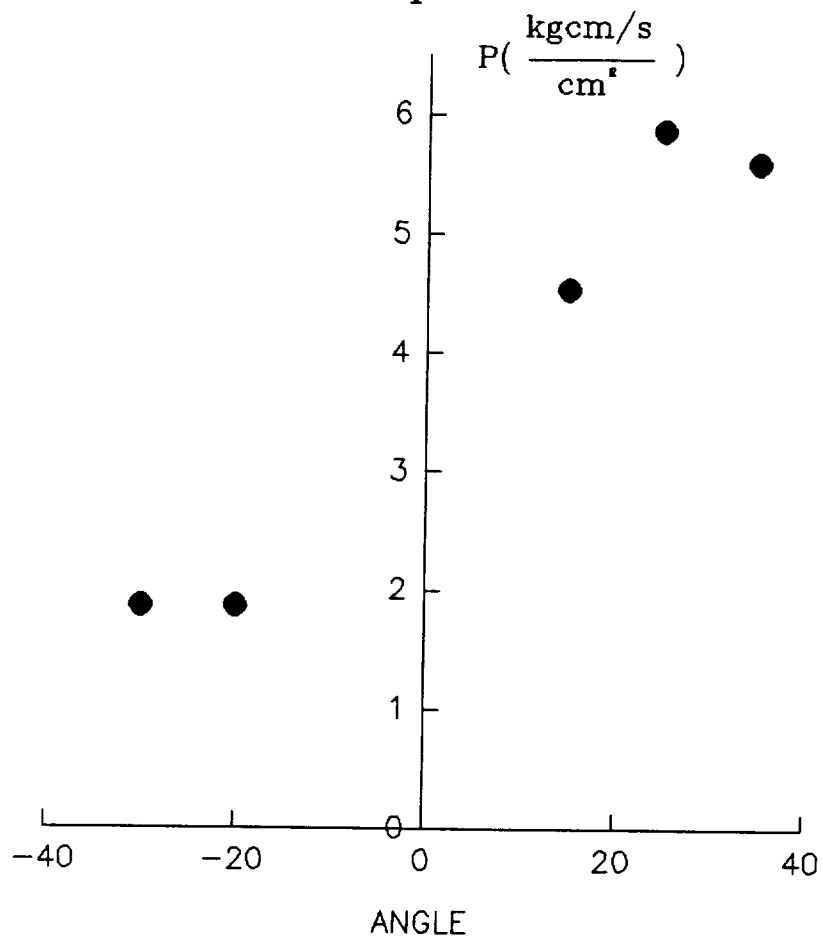


Figure 25. Momentum distribution obtained using the momentum device.

Z-46
0.313" Projectile
7.2 km/s
0.04" Bumper

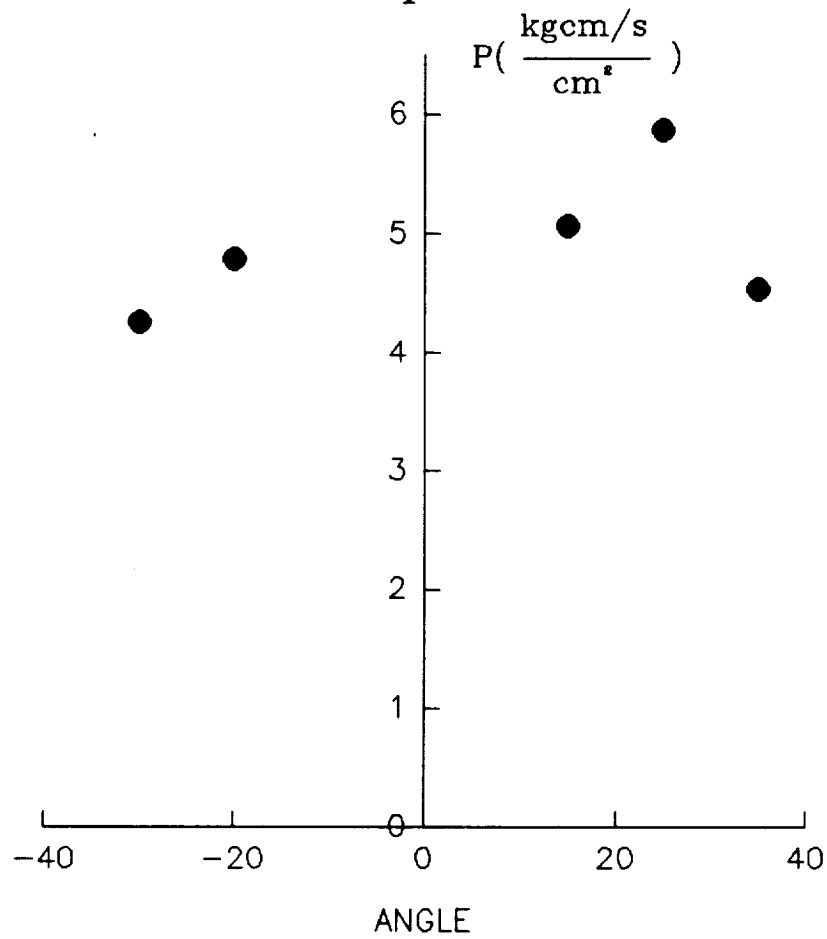


Figure 26. Momentum distribution obtained using the momentum device.

Z-42
0.313" Projectile
6 km/s
0.08" Bumper

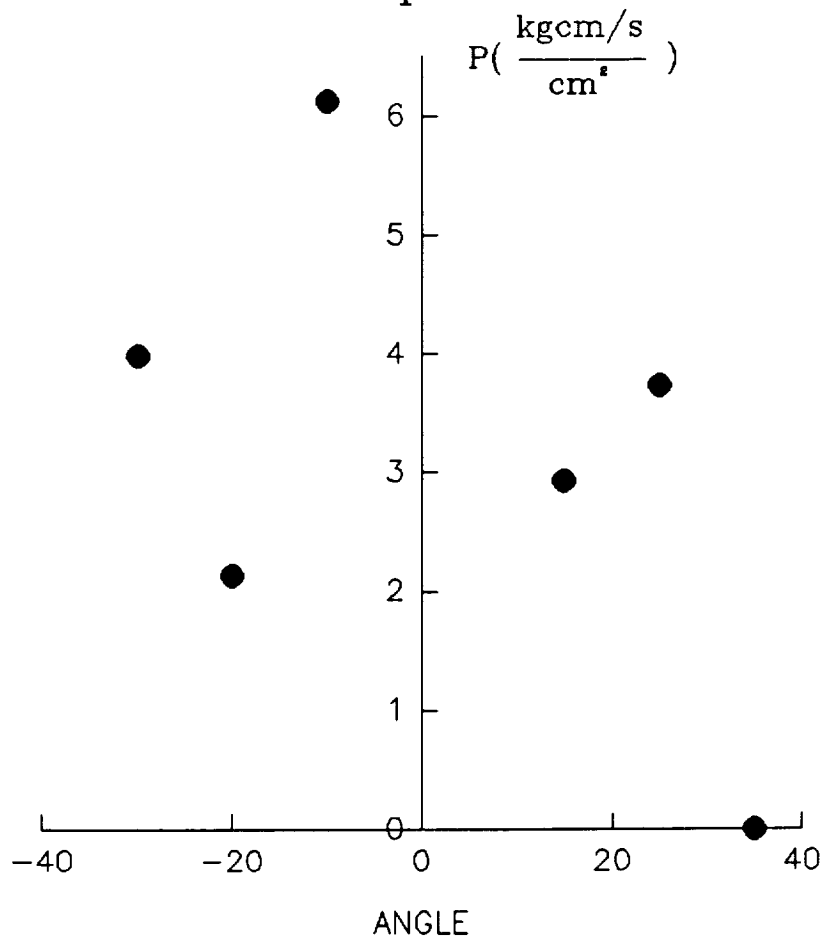


Figure 27. Momentum distribution obtained using the momentum device.

Z-54
0.313" Projectile
6 km/s
0.08" Bumper

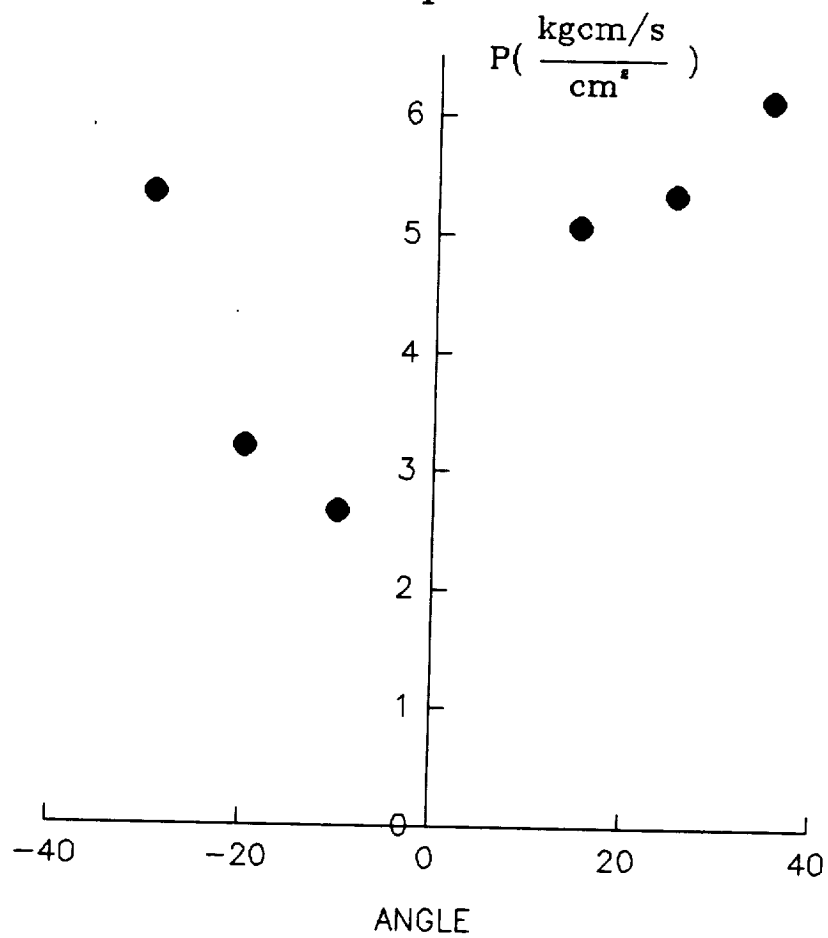


Figure 28. Momentum distribution obtained using the momentum device.

Z-45
0.313" Projectile
7.2 km/s
0.08" Bumper

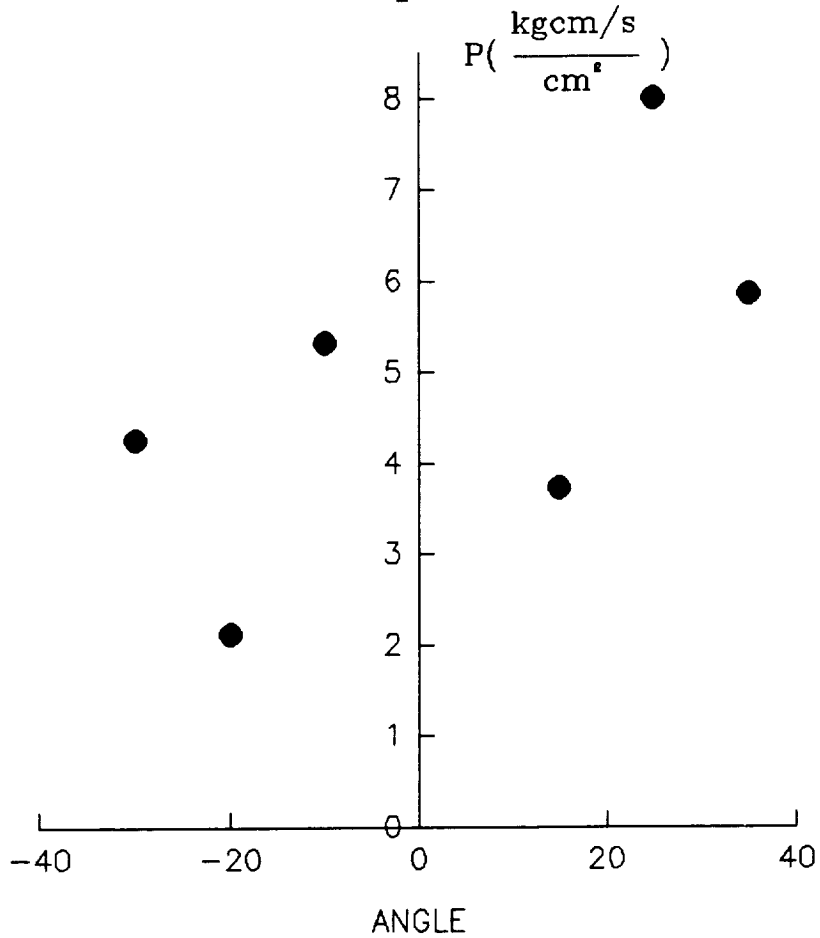


Figure 29. Momentum distribution obtained using the momentum device.

Z-55
0.313" Projectile
7.2 km/s
0.08" Bumper

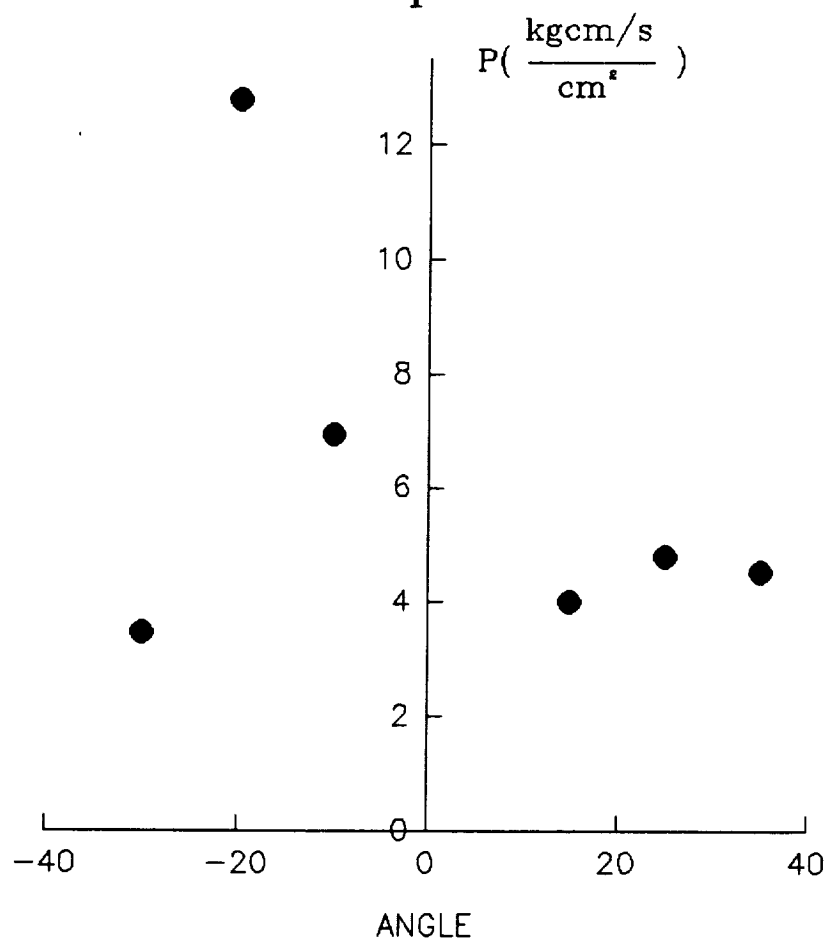


Figure 30. Momentum distribution obtained using the momentum device.

Table 1. Summary of shots conditions

Group	Shot ID	Proj Size (in)	Vel (km/s)	Bumper Thick (in)
A	Z-26	0.25	5	0.04
	*	0.25	5	0.04
	Z-50	0.25	6	0.04
	Z-24	0.25	6	0.05
	Z-47	0.25	6	0.05
	Z-31	0.25	7.2	0.04
	Z-38	0.25	7.2	0.04
B	*	0.25	5	0.08
	Z-39	0.25	6	0.08
	Z-48	0.25	6	0.08
	Z-51	0.25	6	0.08
	*	0.25	6.5	0.08
	*	0.25	7	0.08
	Z-33	0.25	7.2	0.08
	Z-32	0.25	7.2	0.08
C	*	0.313	6	0.04
	Z-44	0.313	6	0.04
	Z-56	0.313	7.2	0.04
	Z-46	0.313	7.2	0.04
D	Z-42	0.313	6	0.08
	Z-54	0.313	6	0.08
	Z-45	0.313	7.2	0.08
	Z-55	0.313	7.2	0.08

* Early shots have no ID assigned to them.

integrating the momentum density as follows.

From the momentum profiles obtained experimentally, we obtain values for P' and r_o . The integration of the momentum density from 0 to r_o gives:

$$P_{tot} = \int_0^{r_o} 2\pi r(P' - Br)dr \quad [10]$$

where r is the radial distance from normal incident and B is the slope of the line connecting r_o and P' .

$$B = P'/r_o \quad [11]$$

Substituting equation [11] into [10] and completing the integration yields:

$$P_{tot} = \pi P' r_o^2 / 2 \quad [12]$$

Where P_{tot} represents the total momentum of the debris cloud. The above calculations assume that the momentum distribution is symmetrical with a dependance on radial distance. This is true for a normal incident impact.

This total momentum calculation was applied to a series of four experiments with small projectiles, as given in Table 2 which lists the values for P' and r_o for each test. These four tests represent two bumper thicknesses and two velocities. More data are needed to facilitate similar calculations for the impacts with larger projectiles due to the discrete characteristics of their debris cloud. Table 3 summaries the results from these calculations. It includes the projectile velocities (v_o), the initial momentum from the projectile ($m_o v_o$), the calculated momentum multiplier. It is evident from these tables that the bumper impact process results in a multiplication of the momentum by a factor of approximately 2.3 to 3.0. This momentum gain does not violate the conservation of momentum since the primary impact also generates backscattered debris which is not measured in this study. Similar results were obtained from the Southwest Research Institute where multiplication factors between 1.44 and 1.76 were obtained. The factors observed in our study were higher since the S_oRI study measured momentum resolved in the incident direction only whereas our study integrates the momentum vectors in the debris cloud in all directions. In addition, the experimental conditions were different between the two investigations. Nevertheless, the presence of a momentum amplification factor implies that the bumper does not reduce the momentum of the secondary debris cloud although it does result in a net loss in energy from the initial impact. Therefore the reduction in the damage on the pressure wall in such a concept must be due to a spreading of the momentum into the presence of the bumper. The exact

dependance of this factor on impact and material parameters can not be determined at this time due to the limited amount of data.

Table 2. Summary of momentum distribution

Shot ID	P' (kg-cm/s-cm ²)	r _o (cm)
Z-38	11.2	6.68
Z-33	4.1	9.79
Z-47	10.2	5.71
Z-51	4.5	8.38

Table 3. Summary of momentum multiplier

Shot ID	Proj. Velocity (km/s)	P _{proj} (kg-cm/s)	P _{tot} (debris) (kg-cm/s)	Momentum Multiplier
Z-38	7.2	260	785	3.0
Z-33	7.2	260	618	2.4
Z-47	6	217	522	2.4
Z-51	6	217	622	2.9

In summary, a system was designed by which the momentum profile through the debris cloud produced during hypervelocity impact may be monitored and analyzed. The objectives were to construct a reliable system which could be utilized several times without major adjustment, to obtain momentum profiles for a given set of test conditions, and to calculate the total momentum present in the debris cloud using the experimentally obtained debris momentum profiles. The system proved to be both reliable and durable. Momentum profiles were obtained and indicated that the data fitting could be accomplished using a triangular approximation. The total momentum calculated revealed a momentum amplification with a multiplier of between 2 and 3. Future work will be done using different projectile sizes and velocities to determine the possible effects of material properties and other variables upon momentum distribution.

Development for Energy Monitoring

An initial design was made for an energy measurement system without any moving components and a device was fabricated. A flat circular plate for catching debris was attached onto a short thin wall cylinder which was in turn rigidly attached to a strong angle brace. The 4" diameter cylinder had a wall thickness of 0.1" and its height was 1". A group of solid state strain gages (minimum of four at 90°) was mounted onto the outside surface of the short cylinder at regular angular interval. During the impact-debris forming process, the debris hitting the target at selected angle will result in measurable strains in the strain gages. Since we are interested in the angular distribution of the energy in the debris cloud, a circular aperture would be appropriate in this geometry. If the momentum distribution of the debris being detected is not symmetrical, then the different strain gages will yield different values. In certain cases, it may even be tensile in nature. The signals from the strain gages will be either collected via a group of strain gage controller or to a group of oscilloscopes. A prototype detector was made but it was quickly realized that results from this device were significantly convoluted so that a precise determination of the energy impacted at a certain angle is almost impossible. Furthermore, this design only allowed one measurement to be made during every shoot. This is very inefficient since only a limited number of shoots can be made for this project. For example, to properly characterize the debris, it is necessary to make at least four shoots. That means, only a maximum of two sets of data can be obtained using eight shoots.

A similar concept was developed which measured energy deposition as a function of scattering angle also using strain gages. We came up with a new

and simpler idea. Individual catcher made of aluminum/steel rod of 1/4" diameter with a larger circular head (3/8") were employed. On each rod, the recoil energy was to be recorded using strain gages. During the impact process, the data will be recorded on an array of oscilloscopes (four oscilloscopes with two channels each). An experiment was conducted to test the sensitivity of various strain gages in terms of response time and gage output. In this experiment, strain gages were attached to aluminum rods. The impact on the rod was simulated by the impact of a hammer. Results from the study shows that the response time may be adequate. In this unit the energy imparted to the sensor can be determined by measuring the response of a set of strain gages mounted on the sensor rod. It is necessary to emphasis that the initial projectile has speeds in excess of 5 km/s, however the debris cloud formed by the initial impact is known to be more spread out in terms of time. Furthermore, even though the debris that the strain gages measure travel at high velocities, the signals from the gages are much slower in time. This is because the speed of these signals corresponds to the natural frequency of the entire recoil device. The response time was found to be in the order milliseconds. This means that a normal strain gage with time resolution in the kHz range is sufficient to resolve the debris energy.

Two types of mounting rods, steel and aluminum, were investigated. These two materials provide different moduli, different yield strength and different work hardening rates. Tests were conducted using different activation processes which include varying forces and durations. Results from the single strain gage in conjunction with a strain gage bridge were very encouraging. The amplitude and the characteristics of the signals from the unit were indeed a function of the impact loading. It was also apparent that

more complex solid state strain gages are not necessary. It was found that the energy measurement devices could be used in two different modes: one based on the elastic behavior of the rod and the other on the plastic deformation. The former method requires a fast response of the sensor as well as the data acquisition system. A set of strain gage amplifiers and an eight-channel data recording unit were temporarily transferred from NASA for this purpose. The plastic deformation method on the other hand needs no real time acquisition. However, due to the none recovery deformation induced by the impact, each sensor has a certain lifetime (in terms of number of impact). For the 1/4"-diameter aluminum rod, it was found that an impact energy of approximately 15J resulted in a permanent strain of approximately 1600 micro-strain. Results from the experiment on aluminum show that even in this soft material, a linear response (and reproducible as well) can be obtained even up to 10 impacts making this time-independent method very attractive. In addition, the deformation response of the rod behaved linearly with energy as expected. A set of experiments was also conducted using steel rods. Under similar impact condition, the strain response of steel was approximately one quarter that of aluminum.

Four types of strain gage configurations were tested: (1) four orthogonally mounted and independent gages, (2) four orthogonally mounted gages which formed an inherent bridge configuration, (3) two orthogonally mounted and independent gages and (4) single strain gage. Each one of these configurations yield different information. Of course configuration (1) would yield the most information but also possesses the most experimental complexity. In the performance tests, it was quickly found that if the energy impacted on the sensor rods was radially symmetrical (that is there was no net

moment on the rod), then all configurations would yield the same information. Results described in the last paragraph were obtained under this condition in which case the simplest configuration (4) would be preferred. However, realistic impact of the debris onto these rod would not be symmetrical in which case bending would occur. In that more complex case, the configuration (1) which consists of four orthogonally mounted gages with independent monitoring is required. Results from off centered shots (asymmetrical impact) confirm this requirement. This more complex configuration will be used in the final device. In all case a pusedo full bridge configuration was used in the strain gage setup. Three external high precision resistors were used to form a full bridge configuration. This, in conjunction with the high gain amplifiers, provides the sensitivity and flexibility needed for the device. It is apparent that more complex solid state strain gages are not necessary.

Tests were conducted to determine the ideal method to extract the information regarding energy density from these unit. Results show that even for steel rods, unless the energy deposition is very low, the large portion of the signal appears in the form of plastic deformation. Based on this information, we decided to concentrate our effort on the determination of energy density of monitoring the permanent strain induced in the sensor. A prototype device consisting of five sensors made of 1/4" diameter steel rods was designed and submitted for machining. A circuit was designed and built to manually zero each individual strain gages.

Energy distribution can also be detected by measuring temperature increase due to impact. Ultimately, energy deposited on a material would be converted to heat. The feasibility of using an infrared thermographic system to measure the surface temperature profile of composite materials under

ballistic impact was demonstrated. Studies have been conducted to characterize the energy absorption mechanisms in composite systems during impact. Infrared thermographic (IR) techniques have been used for non-destructive evaluation of composite materials. The contrast in the thermograph arises from the difference in conductivity and specific heat between the material and the defects. Cielo et.al. were able to distinguish a 0.5 mm thick Teflon sheet in a 10 mm thick graphite-epoxy composite. However, the application of IR thermographic system in determining temperature profile and heat deposition is still very limited. Roberts was able to determine the temperature profile during low velocity impact. However, the profiles obtained were not converted into readable temperature scale using appropriate calibration. In this research, an infrared thermographic system was used to measure the surface temperature profile of composite materials under impact condition similar to that in the debris cloud.

The helium gas gun system was used to provide a velocity of 400 m/s for a projectile of 5 grams in mass. Upon activating the fast acting valve, the charge of helium gas in the gas reservoir propelled the projectile through the barrel of the light gas gun. Composites panels were fabricated using three types of reinforcing fibers (PE, Kevlar and graphite) in an epoxy matrix. The matrix system was epoxy 507 and hardener 956 by Ciba-Geigy. The composite panels were molded in a 216 mm square mold. Each panel was cured under 333 K (60°C) for an hour in the compression molding machine. A ram force corresponding to a pressure of about 0.03 MPa was used. The panels were then cut into 100mmx200mm specimens.

The infrared (IR) thermographic system is shown schematically in figure 31. The temperature distribution was monitored using an IR thermographic

scanner by Inframetrics. The scanner was directed at the center of the sample holder in the gas gun system, as shown in figure 32. Temperature distribution of a line across the point of impact was measured. The temperature distribution data acquired using a Hewlett Packard model 320 computer. The temperatures were measured every 0.25 s until the heat deposited in the composite had completely dissipated. The infrared system was also capable of measuring temperature distribution over an area of the target. This feature would be necessary in the case of non-symmetric sample or impact configurations. However since all the experiments in this present study possessed cylindrical symmetry, the simpler line scan technique was found to be adequate. The operating wavelength of the IR system was 10 μm , which provided the optimum sensitivity at near ambient temperature.

Both baseline scans and calibrations were performed before the experiments were conducted. In the baseline scan, the gas reservoir was discharged without a projectile. The thermographic data were taken for each type of composites. The difference between the actual data upon shooting and the baseline is then the effective temperature profile. All the calculations of heat deposition were based upon the normalized effective temperature profiles.

Calibration was conducted to correlate the intensity of the IR thermographic signals to temperature. As the emissivities of the composites were different, calibrations were performed for all three types of composites. A thermocouple was used to measure the temperature of the composites during calibration. At above room temperature, the samples were heated slowly on a hot plate and readings (both thermocouple and IR intensity) were measured during the heating and cooling processes. For calibration below the ambient

temperature, the samples were first chilled in a refrigerator and the readings were taken during warming. The calibration curve for Spectra-900, Kevlar-49 and graphite composites are shown in figures 33a to 33c respectively. The calibrations were fitted to a linear function and the slope and intercept for the three materials are given in their respective graphs.

Figure 34a shows the typical raw data obtained from the IR thermographic system. All the data were converted using the calibration curves to yield the temperature profiles such as one shown in figure 34b. Note that the "noise" in the curve is a result of difference in thermal conductivity between the fiber and the matrix. The typical error of temperature data is $\pm 1^{\circ}\text{C}$.

The expected variation of temperature with time is shown schematically in figure 35. From t_0 to t_1 , or prior to the impact event, the material was at equilibrium at room temperature. The process between t_1 to t_2 was due to cooling of the target material by the gas in front of the projectile. Beginning from t_2 , the conduction heating from bulk to surface occurred until t_3 where the maximum temperature was reached. The temperature then decreased as a result of heat dissipation. Since the length of the projectile was 5.1 cm and its speed was 260 m/s, the entire penetration process took 0.16 ms. The IR scan was incapable of acquiring data at this rate. The maximum temperature in the temperature versus time plot occurs at approximately 2.5 seconds after the penetration process. This maximum is therefore due to a dynamic balance between the gas cooling effect and the heat conduction from the bulk to the surface.

The temperature versus distance profile across the surface of the sample through the impact point at different times for Kevlar-49 composite impacted by a blunt projectile is shown in figure 36. In figure 36a the sample at

equilibrium was cooled by the gas discharged from the gun barrel. This process corresponds to the interval between t_1 to t_2 as shown in figure 35. During conduction heating from bulk to surface, the measured peak temperature increased, as shown in figure 36b. This process corresponds to t_2 through t_3 in figure 35. Upon heat dissipation, the peak became broader and lower, as shown in figure 36c. This corresponds to the dissipation process from t_3 to t_4 in figure 35.

The surface of the target materials was cooled by the gas stream during impact. Background temperature profiles were obtained by discharging the helium gas without a projectile. Figure 37a shows the background temperature curves for Spectra PE composite at different times. The effective temperature curve could be obtained by superimposing the background on the raw data, as shown in figures 37b to 37d. By subtracting the two curves, the effective temperature profiles can be determined. Figure 38 shows the effective temperature profiles at 1.25 s into the impact process for PE, Kevlar and graphite composites respectively with the gas cooling effect subtracted out. An experiment was also conducted with the IR aimed at the back side of the target (where the projectile exited the target) to examine the difference in the temperature distribution of the two surfaces. The initial cooling of the target by the discharging gas stream prior to impact of the projectile was found to be smaller on the back surface. However, when the background due to this gas cooling was subtracted from the raw signals, the temperature profiles for the two surfaces were very similar. This indicates that the temperature gradient in the thickness direction is unimportant and supports the validity of employing only one IR scanner to monitor the temperature distribution.

INFRARED THERMOGRAPHIC SYSTEM

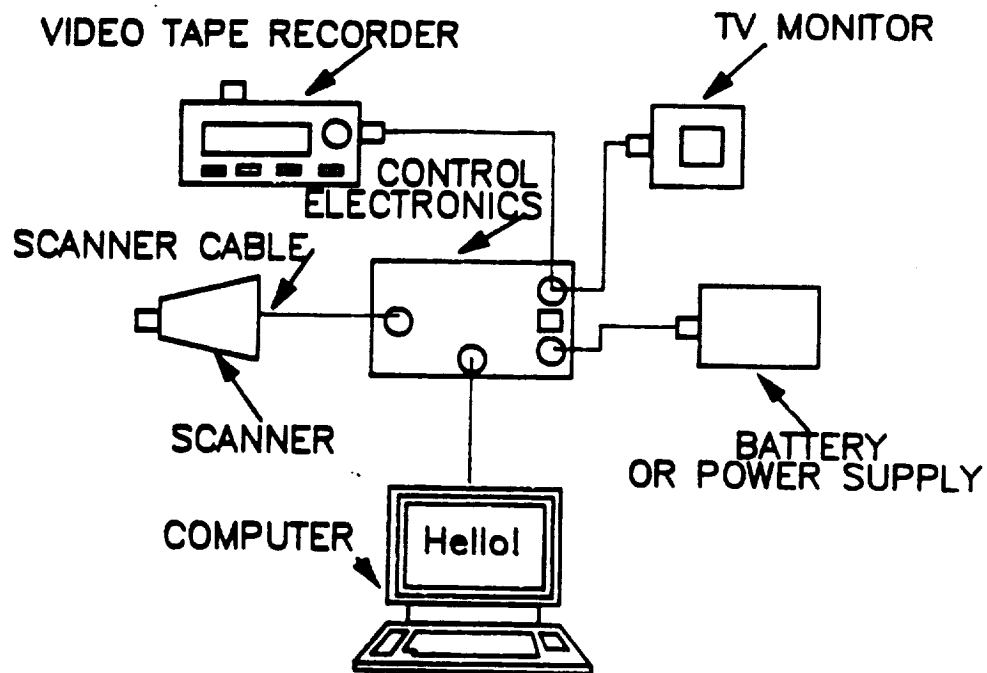


Figure 31. The experimental configuration of the infrared thermographic system for monitoring temperature distribution during impact.

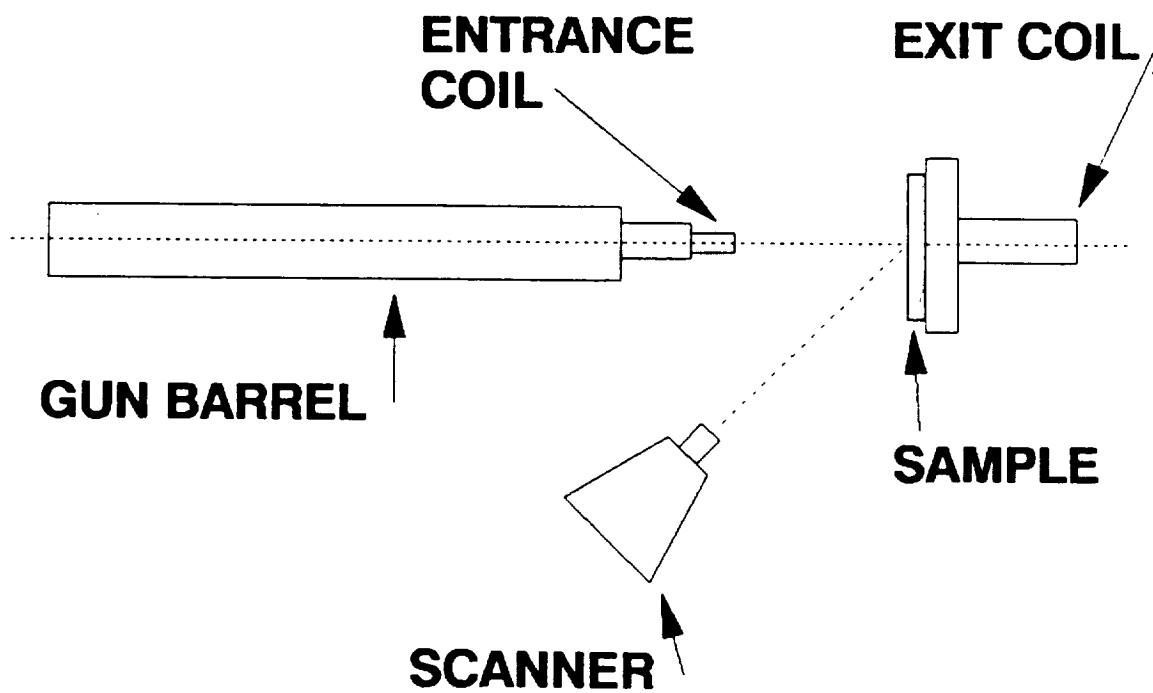
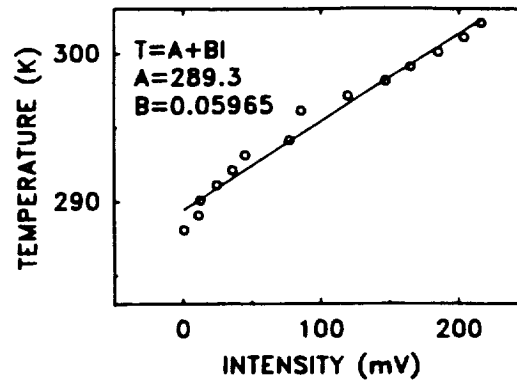
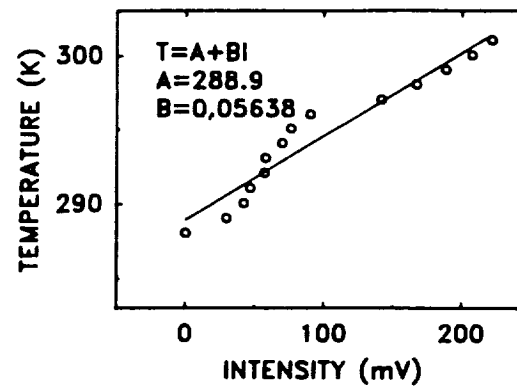


Figure 32. The position of the IR scanner with respect to the gun and the target.

(a) CALIBRATION FOR PE COMPOSITE



(b) CALIBRATION FOR KV COMPOSITE



(c) CALIBRATION FOR GR COMPOSITE

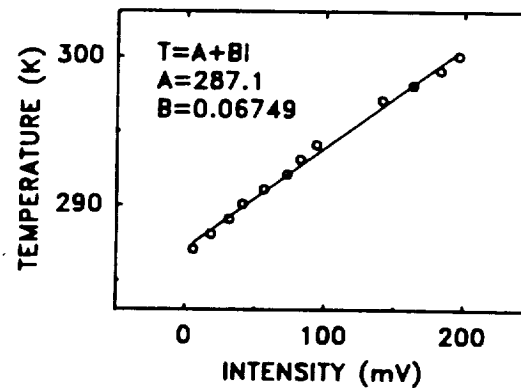


Figure 33. Intensity-temperature calibration for (a) 20-layered Spectra-900 PE composite, (b) 20-layered Kevlar-49 composite and (c) 20-layered graphite composite.

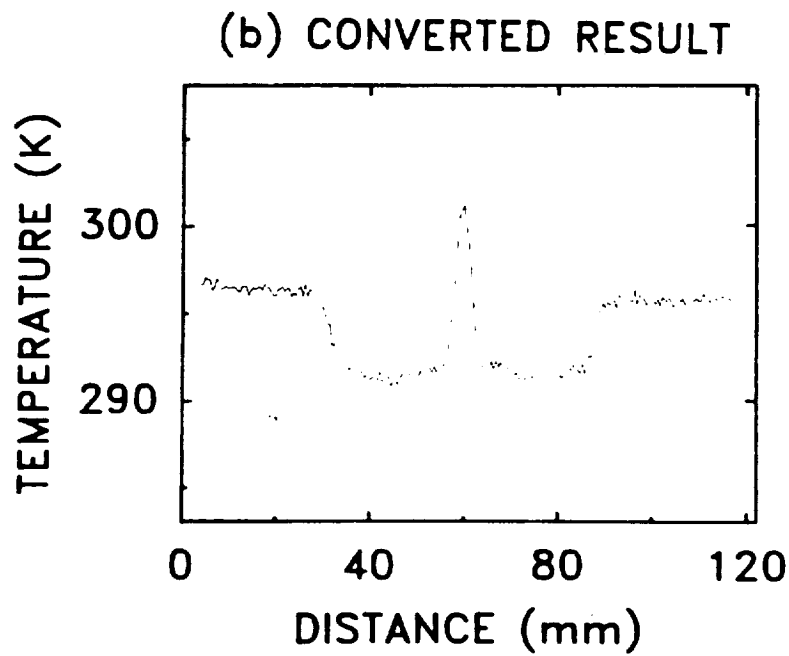
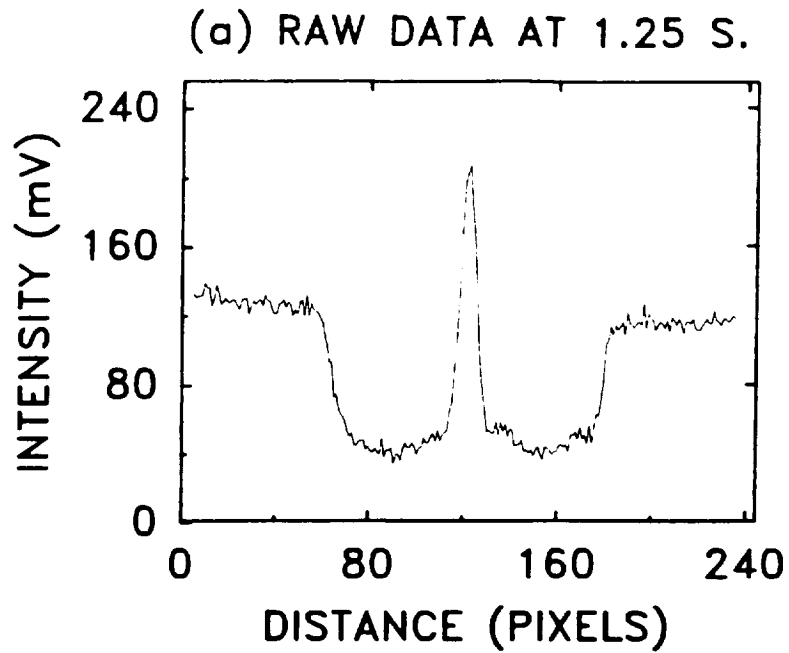


Figure 34. Conversion of (a) raw data in unit of intensity into (b) temperature-distance curve. This set is taken from a PE composite at 1.25 second.

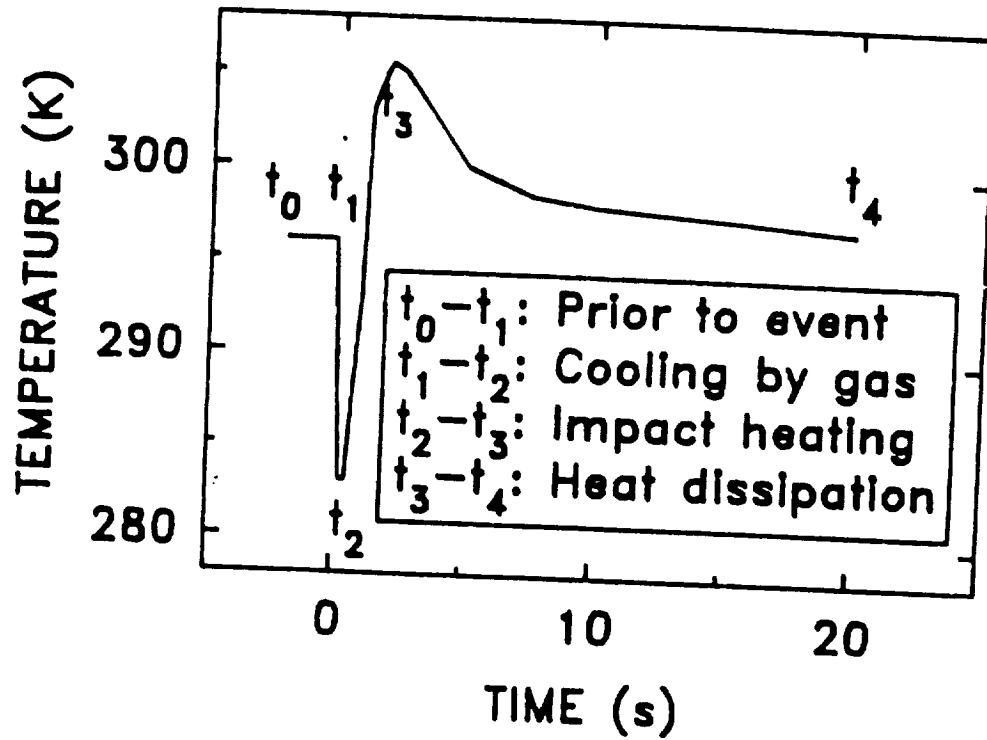


Figure 35. The temperature history showing Kevlar-49 composite impacted by blunt projectiles.

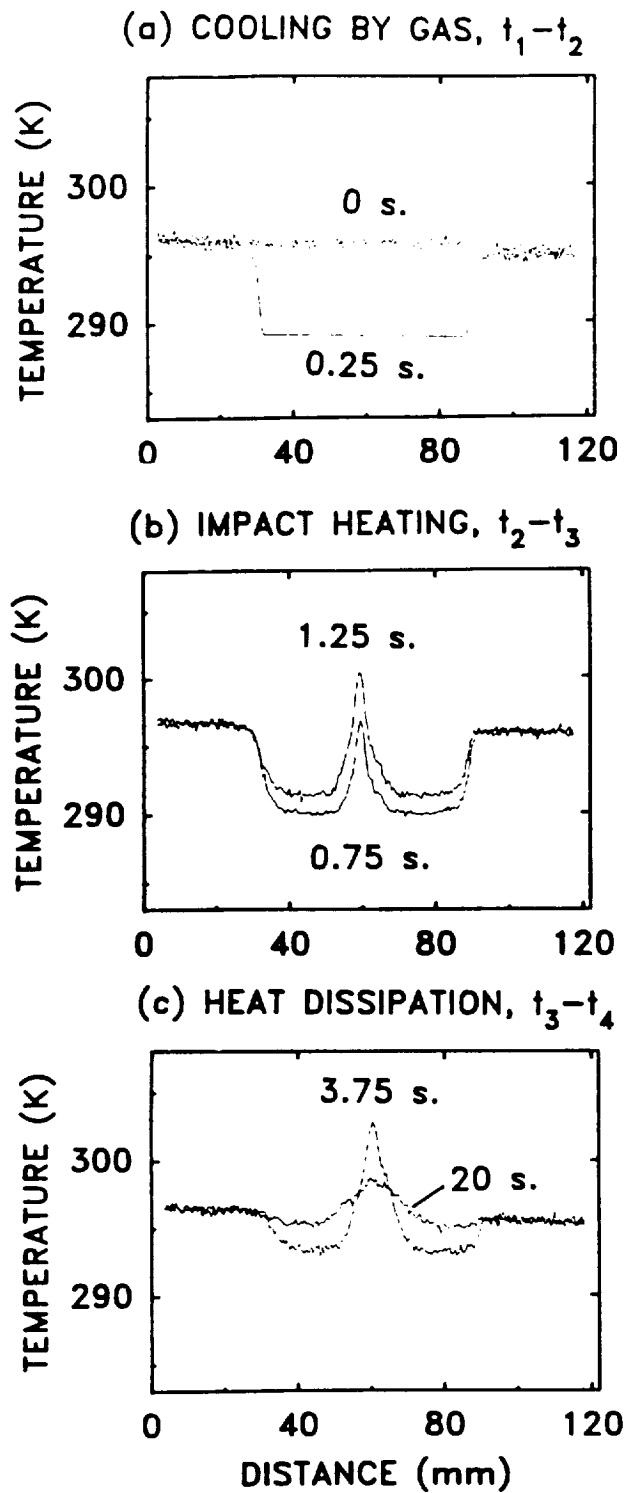
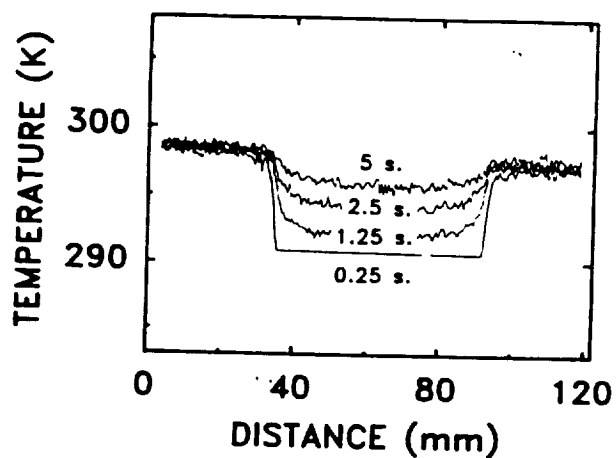
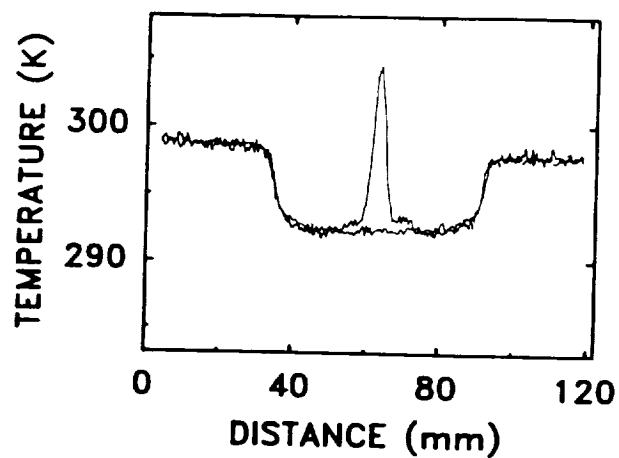


Figure 36. Variation of temperature with time for Kevlar composite impacted by a blunt projectile. (a) initial cooling by air, (b) impact heating and (c) heat dissipation.

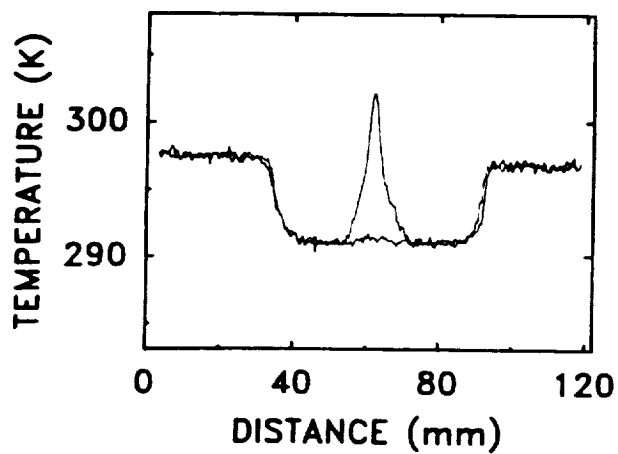
(a) BACKGROUND FOR PE COMPOSITE



(b) PE COMPOSITE



(c) KV COMPOSITE



(d) GR COMPOSITE

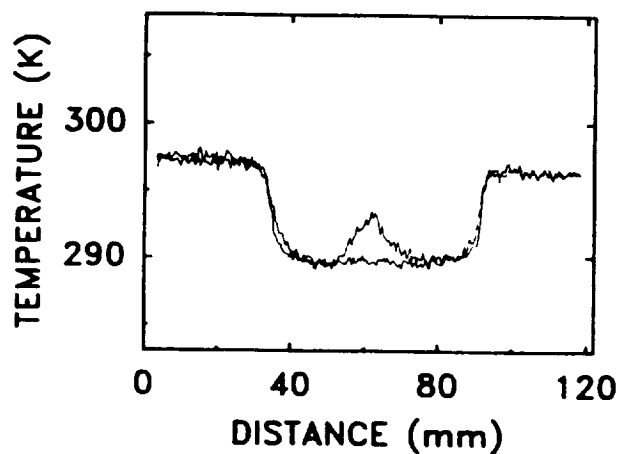


Figure 37. (a) The background curve showing gas cooling for a PE composite.

(b), (c) and (d) are overlaid curves for the temperature profiles and the corresponding background for PE, Kevlar and graphite composites respectively at a time of 1.25 second.

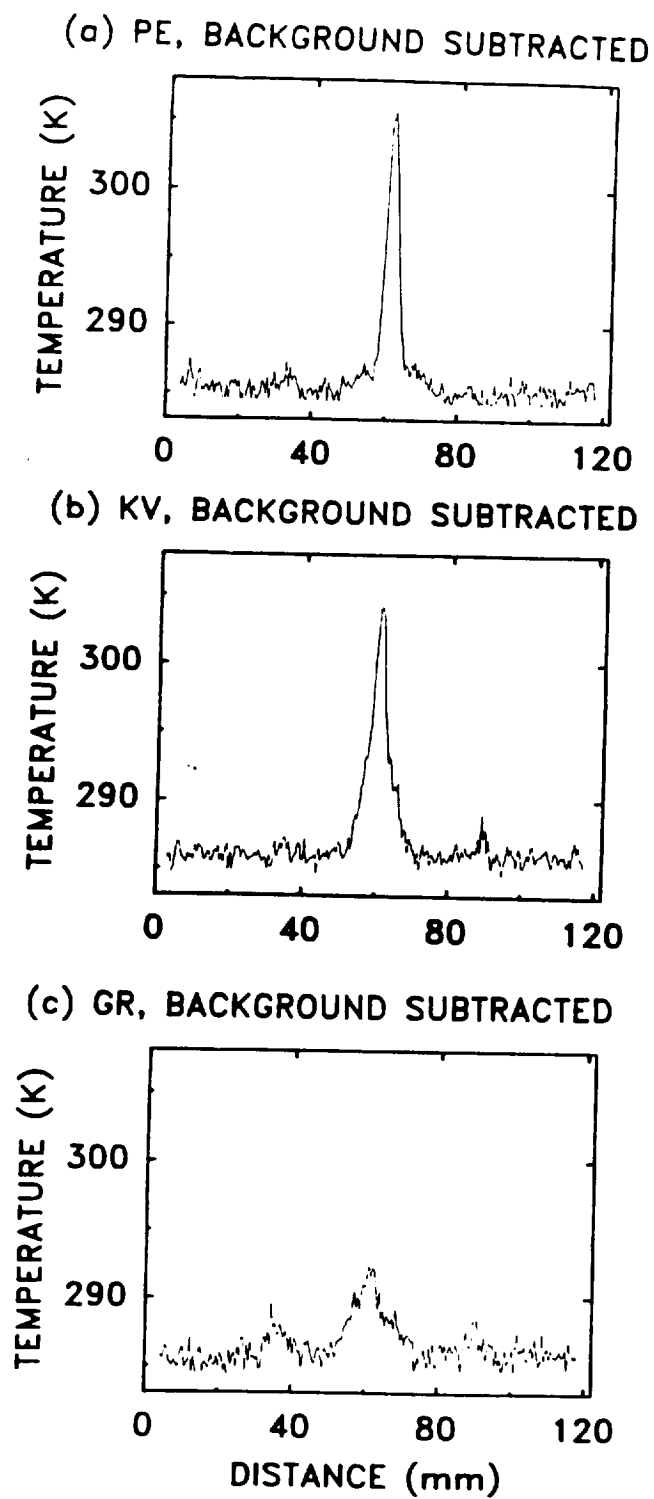


Figure 38. Effective temperature profiles with the background subtracted for (a) PE Spectra-900, (b) Kevlar and (c) graphite composites respectively.

CHARACTERIZATION OF ENERGY LOSS IN ADVANCED MATERIALS FOR SECONDARY PROTECTION

It has been demonstrated that energy can be effectively dissipated in augmented configurations using advanced composites. The objective of this study is to determine the energy dissipation processes in polymer-matrix composites during impact conditions similar to that experienced by the pressure wall due to the debris cloud. These processes include heat, fiber deformation and breakage, matrix deformation and fracture and interfacial delamination. In this study, experimental measurements were made, using specialized specimen designs and test methods, to isolate the energy consumed by each of these processes during impact in the ballistic range. Using these experiments, relationships between material parameters and energy dissipation were examined. Composites with the same matrix but reinforced with Kevlar, PE and graphite fabric were included in this study. These fibers were selected based on the differences in their intrinsic properties. Matrix cracking was found to be one of the most important energy absorption mechanisms during impact, especially in ductile samples such as Spectra-900 PE and Kevlar-49 reinforced polymer. On the contrary, delamination dominated the energy dissipation in brittle composites such as graphite reinforced materials. The contribution from frictional forces was also investigated and the energy partitioning among the different processes evaluated.

Three types of such materials were selected for this research: PE Spectra-900 for its high strength, high ductility, low modulus and low specific gravity; Kevlar-49 fiber for its high strength, medium ductility and specific gravity and low modulus; and graphite for its high tensile modulus and low ductility. Only one resin material (Epoxy 507 and hardener 956 by Ciba-Geigy) was used because of its availability and ease of processing. The

diameter of the PE fibers was 38 μm , that of Kevlar was 12 μm and that of graphite was 7 μm . The numbers of fibers per strand were 118, 768 and 3000 in PE, Kevlar and graphite respectively.

All the composite panels were molded in a 216 mm square mold. Each panel was cured under 333 K (60°C) for an hour in the compression molding machine. A ram force, corresponding to a pressure of about 0.03 MPa, was used. The panels were then cut into 100mm x 200mm specimens. In the experiments to study the effect of delamination, a stacked single layer geometry was used to simulate a delaminated composite structure. In this case, single layer sheets were made by inserting polypropylene sheets in between layers. The panels were then separated into individual composite sheets. The difference in total energy absorption between the composite panels and the corresponding separate stacked sheets was assumed to be the contribution from the delamination process.

Samples for fiber tests were made by winding each end of the fiber strand around an aluminum tab. Adhesives were applied along the fiber strands on the aluminum tabs. Care was taken to ensure the gauge length was 63.5 mm (2.5 inches). It was found that fiber samples prepared in this manner provided less slippage and hence more accurate gauge length than other sample configurations. In these fiber experiments, a special projectile tip was used to eliminate slippage of the projectile in between yarns. The number of fractured fiber strands were evaluated by a post-mortem examination of the samples. The energy absorbed by the fibers was calculated by multiplying the energy absorbed by an individual strand by the number of broken fibers.

Frictional forces between the projectile and the material is the source of energy dissipation after the target has been perforated. This contribution

is usually a secondary effect. Nevertheless, its contribution is not negligible in elastic materials. A sample holder bracket was designed to hold the specimen in exactly the same position. The energy loss of the projectile passing through the same hole a second time is directly related to this frictional energy. The data obtained from this test were used to compare with the frictional loss measured from the original tests. The contribution of friction to the total energy absorption of each composite system was then evaluated.

The volume fractions of the fiber in the composites were determined using quantitative optical microscopy. The fiber volume fractions for graphite and Kevlar-49 composites were found to be 54.7% and 55.4% respectively. Because polyethylene fiber has a much higher ductility than the matrix system, the polished surface revealed only broken fiber ends without any matrix. Consequently quantitative microstructural analysis was not an appropriate method of determining the volume fraction of PE fiber in the composite. Since all the composite panels were molded with the same pressure and all the fibers used were in the same (plane weave) form, it is reasonable to assume the fiber volume fraction for PE composite to be 55%. Density measurements of all the composites (including PE composites) were also made and their results agreed well with the optical measurements.

In all the tests, a steel projectile tip was used for the projectile to ensure minimal plastic deformation so that energy loss measured can be attributed to target deformation. A conical shape with an angle of 50° was used for the tip. A projectile velocity of 280 m/s was used in all the tests.

The most important issue to be addressed is the total energy absorption of the composites during the penetration process. The total energy absorption

qualifies a composite material for ballistic impact applications. The major energy absorption mechanisms include fiber deformation and breakage, matrix cracking, delamination process and frictional loss. The contribution from each of these mechanisms was investigated and determined quantitatively.

Figures 43, 44 and 45 show the energy profiles of PE, Kelvar and graphite composites and are representative of all the materials examined. Each figure contains data from two shots, denoted by open and filled circles respectively. As shown in these figures, total energy loss values obtained from these experiments are very consistent between shots. It is important to note that the data in figures 43 to 45 represent the positional dependence energy loss as the projectiles traverse through the targets. The range at which energy is lost occurs over a longer distance than the thickness of the target. This is because the energy dissipation process begins at the point of contact and ends when the projectile exists material. The total energy loss process can be divided into two stages. The initial rapid energy loss is due to the fracture of the target. This starts at the moment of contact and finishes when a hole is formed. This is followed by a more gradual loss due to friction. Polyethylene reinforced composites exhibited a smoother behavior than graphite composites because the total energy loss in the former is larger. With the same absolute error value, the percentage error in the PE composite is proportionally smaller than the graphite counterpart.

Figure 46 summarizes the data obtained from Spectra-900 PE, Kevlar-49 and graphite composites respectively, each composed of 10, 20 and 30 layers. The total energy absorption was found to be approximately proportional to the thickness of the composite (or the number of layers). This implies that the energy loss rate is independent of the thickness of the target, at least

within the range of thicknesses investigated. It appears that this linear relationship applies regardless of the fiber properties, although graphite is a high strength but brittle fiber, whereas Kevlar and PE have lower moduli but higher ductility. Figures 47a and 47b show the data normalized to sample thickness and weight instead of the simple absolute energy loss values. The Spectra-900 PE composites possess the best energy absorption density. This is because PE fiber has the lowest specific weight and highest ductility. Nevertheless, the full potential of the ductility of PE and Kevlar fibers was not realized due to the restriction imposed by the matrix. This restriction limits the deformation of the ductile PE and Kevlar fibers to regions in the vicinity of the impact. The damaged region could be expanded by using unidirectional fiber reinforced composites. The stress wave will travel over a greater region in this type of composites. However, the degree of fiber breakage will decrease because the shear force acting on the fiber by the projectile is lower.

The energy absorption process can be divided into two parts, namely energy of penetration and frictional energy. The energy of penetration includes contributions from fiber deformation and breakage, matrix cracking, delamination and debonding. The average penetrating force can be determined from the slope of the energy-position curve. The average force required to penetrate the composites increases with increasing target thickness as shown in Figure 48. There is a near linear relationship between the penetrating force and sample thickness for graphite composite, but the PE and Kevlar composites exhibit a positive deviation from linearity. The average force of penetration can be simulated by a parallel array of spring-dashpot systems. The single-layered composite can be represented by a model of spring constant,

k , and dashpot constant (damping coefficient), c . The equation of motion can be written as $c\dot{x}+kx=F_1$ where x is the displacement vector and \dot{x} the velocity vector. Hence, the force required to penetrate n layers, F_n , can be written as $n(c\dot{x}+kx)=F_n$. Combining the two equations, we have $F_n=nF_1$. This Maxwell model predicts a linear relationship between the average force of penetration and the number of layers. For a brittle composite such as graphite, the plastic deformation is negligible, the elastic model thus accurately predict the behavior of the material. However, for ductile materials such as Spectra-900 PE and Kevlar-49, the plastic deformation is not negligible. The damping coefficient becomes progressively higher in thicker samples resulting in a positive deviation from linearity in the force-thickness relationship observed in these materials.

A series of experiments were conducted to determine the intrinsic properties of the fibers used in this study in order to determine the fiber contribution to energy absorption. The samples for all the fiber tests were prepared in the same manner to ensure consistent testing conditions. The number of strands in each sample were 20, 15 and 10 for graphite, Kevlar-49 and Spectra-900 PE fibers respectively. The number of fiber strands used in this experiment was the maximum amount of fibers that the projectile could interact with. The fiber strands were twisted 2 turns/cm (5 turns/inch) to form a bundle. This sample configuration helped prevent slippage during impact. Only those samples in which all fibers broke at the center were included in the analyses. Data from samples with fracture away from the gauge length or partially broke were not included. A projectile velocity of 280 m/s was used.

The energy loss values for Spectra-900 PE, Kevlar and graphite fibers

under this high velocity test condition were 0.7, 0.7 and 0.4 J/strand respectively. Normalizing these values to the volume of the fiber yielded energy absorption densities of 82.4, 127 and 54.5 J/cm³ for the three respective fibers. These values are related to the toughness of the fibers which in turn is proportional (upper limit) to the strength-ductility product of the materials. According to the manufacturers' specifications, the toughness values of the three fibers of interest are 90.6 J/cm³ for PE, 78.4 J/cm³ for Kevlar and 37.2 J/cm³ for graphite. A direct comparison of these calculated toughness values with the energy absorption densities shows that the Kevlar and graphite fibers are capable of absorbing more energy under the impact condition than expected. An inspection of the broken fibers reveals that the elongation observed is higher than expected. The elongation was about 5% in the Kevlar fibers and about 2% in graphite implying a strain rate sensitivity of the deformation process.

The total energy absorption of the fibers can be calculated by multiplying the measured energy density values by the volume of the fibers in the fracture zones of the composites. The average size of the fracture zone was 9.53 mm. The thickness of 20-layer thick composites was 8.4 mm, 5.5 mm and 5.4 mm for PE, Kevlar and graphite composites respectively. Using the volume fraction of the fibers and the thickness of the 20-layer composite, the energies consumed to damage the fibers within the fracture zone were determined to be 23.7 J for PE, 23.9 J for Kevlar and 10.1 J for graphite. The contributions from fiber energy in the total energy absorption of the PE, Kevlar and graphite composites were 35%, 58% and 19% respectively.

In this analysis, the energy dissipated by fiber pull-out (which is affected by fiber size) and the energy dissipated by those fibers that

deformed outside the fracture zone but not break were ignored. This implies that the analysis underestimates the total amount of energy dissipated. To successfully isolate the contribution from fiber pull-out, experiments using controlled interfaces and different fiber sizes are needed. This is beyond the scope of the present investigation. Post-mortem examination of the fracture zones in all three composites reveals that most of the fibers that participate in the energy absorption process are broken. This indicates that under ballistic impact condition, the energy dissipated in straining the fibers that do not break is insignificant.

Initially, the energy loss due to matrix cracking was studied using pure resin materials (without fibers). It was determined that the damage characteristics from this unreinforced material did not resemble those observed in composites. The extent of matrix cracking in a composite is different from that in the pure resin. Hence, the energy absorbed for matrix cracking depends on fiber reinforcement and is not the same in the three composite systems. A new test methodology was then developed to measure the fiber contribution using composite samples with different volume fractions of matrix material. This was accomplished by fabricating and testing composites with identical amount of fabric but different amounts of resin. The amount of excess resin was small enough so that the flexural rigidity of the composites was not altered in a significant manner. Effort was concentrated on the PE, Kevlar and graphite composites each with 20 layers of fabric. One set of samples were fabricated in a normal fashion whereas excess resin was intentionally added to the thicker samples. Care was taken to introduce the excess resin uniformly in between layers. The thick samples have a higher volume fraction of matrix than the standard samples have. The difference in

energy absorption between the two is then the contribution from the matrix and the results were normalized to reflect only the matrix contribution. The graphite, Kevlar and PE materials have normalized matrix cracking energies of 56, 66 and 71 J/cm of resin respectively. Using the fracture zone morphology of the three types of samples, these energies correspond to energy absorption densities of 78.5, 92.5 and 99.5 J/cm³ respectively for graphite, Kevlar and PE composites. For comparison, the energy absorption density of pure resin (without fibers) was found to be 21 J/cm³. This implies that the presence of fiber strongly enhance the energy absorption capability of the resin due to a complete change in the damage morphology in the composite structure as opposed to a homogeneous resin system.

The energy of matrix cracking in a composite can be evaluated from multiplying the normalized matrix cracking energy by the volume of the resin in the composites. This requires evaluating the volume fractions of the fibers and the matrix. Using the approach similar to that given in determining fiber volume fraction of the composites, the equivalent resin thickness for 20-layer thick composites were determined. The energy absorption of resin was then calculated to be 26.8 J for PE, 16.4 J for Kevlar and 13.5 J for graphite composites. The contributions from matrix cracking in total energy loss were 40%, 40% and 25% for PE, Kevlar and graphite composites respectively. However, the increase in energy absorption as a result of thicker resin cannot be completely attributed to matrix cracking. The effect of higher frictional loss in the thicker samples must also be taken into consideration. The frictional partitions in total energy absorption for 20-layer thick composites were determined to be 16.4%, 11.1% and 19.6% for Spectra-900 PE, Kevlar-49 and graphite composites respectively. This

frictional contribution will be discussed later in the paper. Thus, the contributions from matrix cracking, excluding frictional component, were 33%, 35% and 20% for Spectra-900 PE, Kevlar and graphite composites respectively.

The effect of delamination was investigated by comparing the response of normally fabricated composites where delamination can occur with materials where delamination was eliminated from the energy absorption process. The latter was achieved by stacking individual layers of the composite sheets together, which simulated the delaminated structure of the composites. Data from these experiments are shown in Figure 49. The difference between the energy absorbed by the two configurations yields the energy consumed by delamination. The effects of delamination appear to be minor in the Kevlar and PE composites, whereas the delaminated graphite-based materials absorb less energy than their composite counterparts. The stacked composite sheets were found to be thicker than the composite panels of the same number of layers. Since both types of samples used had the same number of fibers, the difference in thickness could be attributed to the difference in resin thickness. The energy loss of the delaminated samples can then be normalized by subtracting the contribution of the excess matrix energy from the total energy loss. The data listed in Table 4 are the corrected delamination energies. These values suggest that the delamination process is the governing energy absorption mechanism for graphite composites. This accounts for 62% in total energy loss for 20-layer thick graphite composite and over 46% in the 30-layer material. The PE reinforced composites exhibited the least energy loss by this mechanism (5.1% in 30 layers to 1.5% in 20 layers). The -3J observed in the 10-layer PE is due to a combination of the low energy absorption by delamination and systematic error of the measurement ($\pm 3J$). The

total delamination area can be evaluated by dividing the normalized delamination energy by the shear-mode fracture toughness, G_{IIC} , of the composites. These values correspond to 0.15 J/cm^2 for graphite composites, 0.09 J/cm^2 for Kevlar and 0.014 J/cm^2 for PE. The total delamination area was found to be 243 cm^2 , 231 cm^2 and 357 cm^2 for 30-layer thick graphite, Kevlar-49 and Spectra-900 PE composites respectively. Hence, the average diameter of delamination, assuming a circular shape, was 3.3 cm, 3.2 cm and 3.9 cm for graphite, Kevlar-49 and Spectra-900 PE composites respectively. These delamination sizes agree with the damage zone observed in the impacted materials. Results from these delamination energy experiments suggest that the delamination process is the most important mechanism for graphite composite followed by Kevlar and PE composites. This is due to the low energy dissipation factor in the inplane shear mode in the PE rather than the ability of the material to generate delamination. It is controversial whether delamination is the governing mechanism of a composite under impact penetration conditions. Some researchers have suggested that strain energy at failure of the fibers is the controlling factor of the impact response of composites, whereas Wrzesian remarked that, "Panels with good penetration resistance were heavily delaminated, indicating that a considerable amount of energy was absorbed by the delamination". Results from this research suggest that the effectiveness of delamination as a means to dissipate energy is a function of the fundamental properties of the composites, such as the ductilities of the fibers and the matrix. Wrzesian's position is therefore valid only for graphite composites and not for the other two systems.

The contribution from frictional loss during high velocity impact was determined from the frictional component of the energy-position curves. The

frictional process starts with the point of perforation and ends with the complete passage of the projectile. The energy loss during this interval was taken as the frictional loss.

The frictional loss is proportional to the normal force and the coefficient of friction between the two contacting materials. The frictional energy loss in each type of material was thus quite different. Since graphite composites fracture by fragmentation, the area of contact between the two materials is very limited and unstable, especially for thinner samples. Postmortem examination of the graphite samples reveals that part of the target material forms debris and disintegrates upon impact. Spectra-900 PE composites, on the other hand, fracture in a mode involving the growth of a ductile zone. This ensures a constant contact between the target and the projectile materials. As a result, a well behaved trend in frictional behavior was observed in Spectra-900 PE composites, whereas greater fluctuations were encountered in the graphite materials.

The contributions from frictional energy in each type of material are listed in Table 5. Results from these experiments reveal that the frictional component accounts for 20-21% of the energy absorption in graphite composite, 11% in Kevlar-49 composite and 14-16% in Spectra-900 PE composite.

Table 6 summarizes the fractional contributions from each of the four different energy dissipation processes determined from the experiments conducted in this study for the 20-layer and the 30-layer composites. The delamination process was found to be the most important mechanism in graphite composites. For Kevlar-49 and Spectra-900 PE composites, the fiber breakage and matrix cracking are the governing energy absorption mechanisms. The experimental error in measuring the energy loss is ± 3.5 J. The cumulative

error range in summing up the four mechanisms is therefore ± 14 J. The error in estimating the energy contributions thus decreases with increasing total energy. The methodology developed in this study of partitioning the energy absorption in a composite system is very useful. The relative contribution from each energy absorbing mechanism can be determined. Higher precision can be achieved by improving the sensor and/or the sensitivity of the micro-velocity sensor.

The total energy loss can be written as

$$E = E_{\text{fiber}} + E_{\text{matrix}} + E_{\text{delamination}} + E_{\text{friction}} \quad [13]$$

As a result of the present findings, it is now possible to quantify these energy loss processes. The sum of the four individual contributions does not equal to unity since the fractional contributions were determined by independent experiments. The deviation from unity arises from the intrinsic error associated with the experiments and the mutual interaction between the various components that the study is unable to account for. According to Table 6, the sum of the individual energy absorption factors ranges from 87% to 124% of the total energy loss measured. These values are within the systematic error of the measurement scheme.

It is impossible at this stage to analyze the energy partitioning behavior from a first principle approach. Nevertheless several characteristics are evident from the data obtained in this study. It appears that in brittle composites (graphite), the single most dominating energy absorption process is delamination. However, this is due to the large energy release density and not because of the ability of the graphite composite to delaminate. On the contrary, composites reinforced with ductile fibers tend to dissipate energy via fiber deformation and matrix cracking as expected. In

addition, generation of friction during the passage of the projectile also contributes significantly to the energy absorption process in all three composites.

In summary, energy loss during the penetration of ballistic projectiles was experimentally measured for composites with different reinforcements (including Spectra-900 PE, Kevlar-49 and graphite). The partitioning of this energy among four distinctive modes was determined. These modes include fiber deformation and breakage, matrix fracture, delamination and friction. Results indicate that the energy partitioning behavior is a complex and interactive function between the fibers and the matrix. A simple correlation of the toughness of the individual components (fiber and matrix) does not exist for the composite structure. Delamination plays an important role in brittle composites as a result of the large energy release from such a process. For ductile materials, the contributions from the fibers and the matrix are more important. This information can be incorporated to aid the design of more effective augmented bumpers.

Table 4. Corrected Delamination Energy

	Graphite Composite	Kevlar-49 Composite	Spectra-900 PE Composite
10 Layers	12 J	0 J	-3 J
20 Layers	33 J	8 J	1 J
30 Layers	37 J	21 J	5 J

Table 5. Energy Absorbed by Friction in 20-Layer Composites

Graphite Composite	Kevlar-49 Composite	Spectra-900 PE Composite
19.6 %	11.1 %	16.4 %

Table 6. Summary of the Contribution from each Mechanism to Total Energy Loss

20 Layers

	Graphite Composite	Kevlar-49 Composite	Spectra-900 PE Composite
Fiber	19.1 %	58.3 %	35.4 %
Matrix	20.5 %	35.5 %	33.4 %
Delamination	62.3 %	19.5 %	1.5 %
Friction	19.6 %	11.2 %	16.4 %
Total	121 ± 27 %	124 ± 36 %	87 ± 21 %

30 Layers

	Graphite Composite	Kevlar-49 Composite	Spectra-900 PE Composite
Fiber	20.3 %	47.8 %	35.7 %
Matrix	19.3 %	27.2 %	32.5 %
Delamination	46.3 %	28.4 %	5.1 %
Friction	21.3 %	10.8 %	13.5 %
Total	107 ± 17 %	114 ± 19 %	87 ± 14 %

PE COMPOSITE, 20 LAYERS

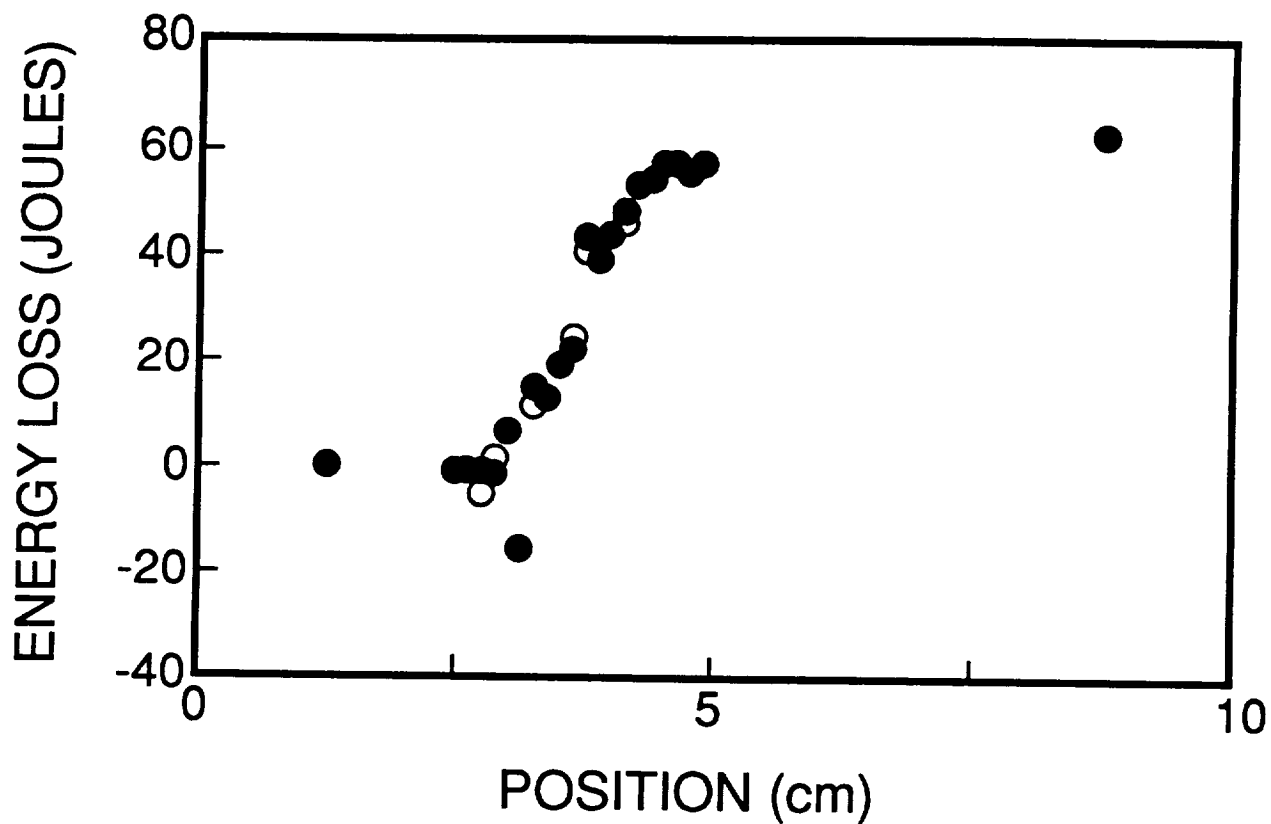


Figure 43. Energy loss versus position curve for a Spectra-900 PE composite.

KEVLAR COMPOSITE, 30 LAYERS

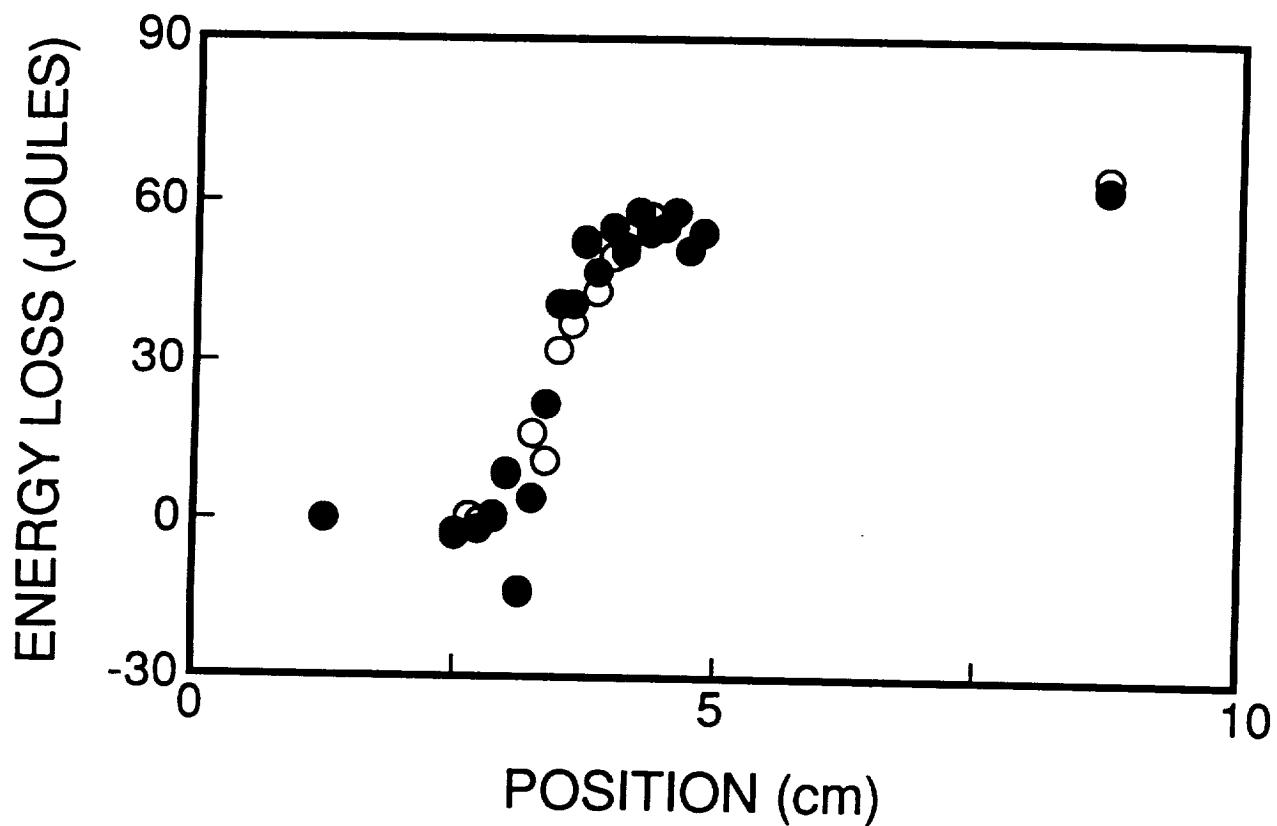


Figure 44. Energy loss versus position curve for a Kevlar-49 composite.

GRAPHITE COMPOSITE, 20 LAYERS

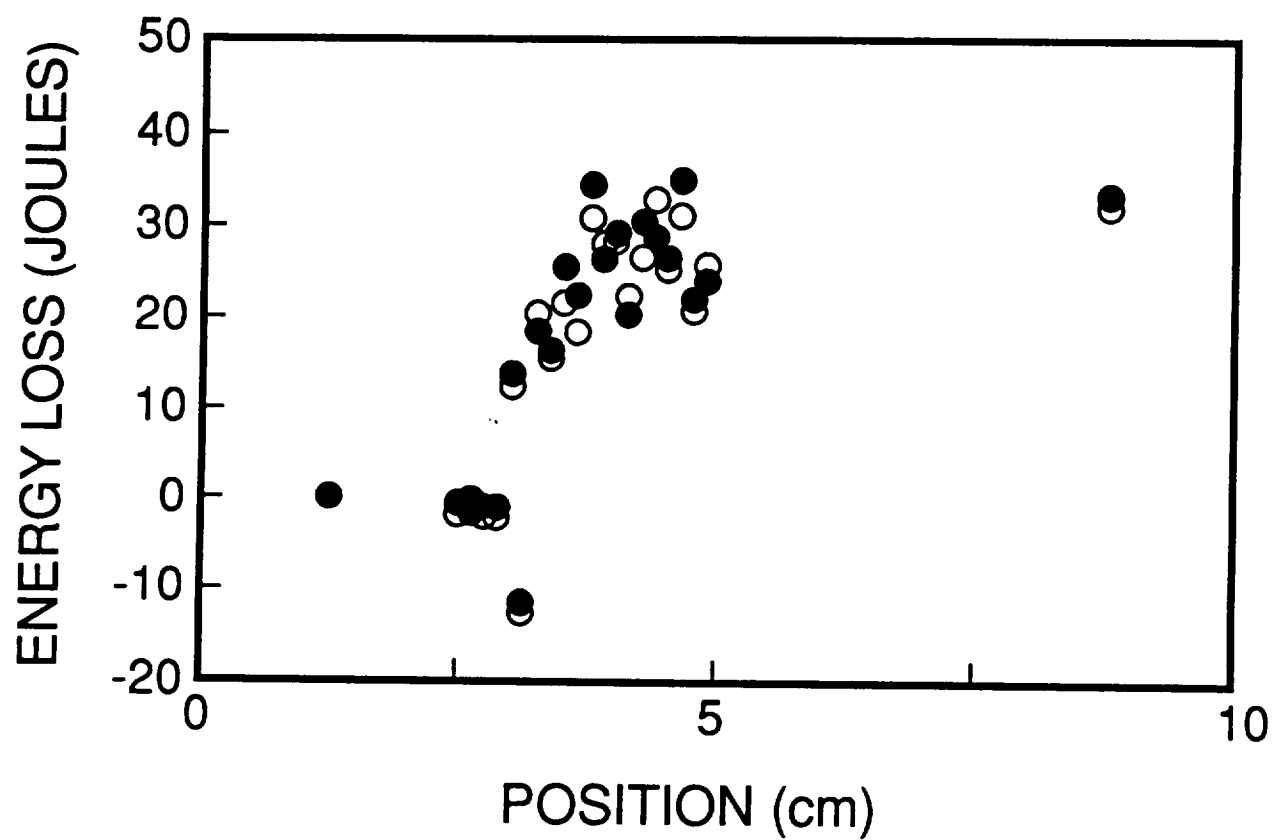


Figure 45. Energy loss versus position curve for a graphite composite.

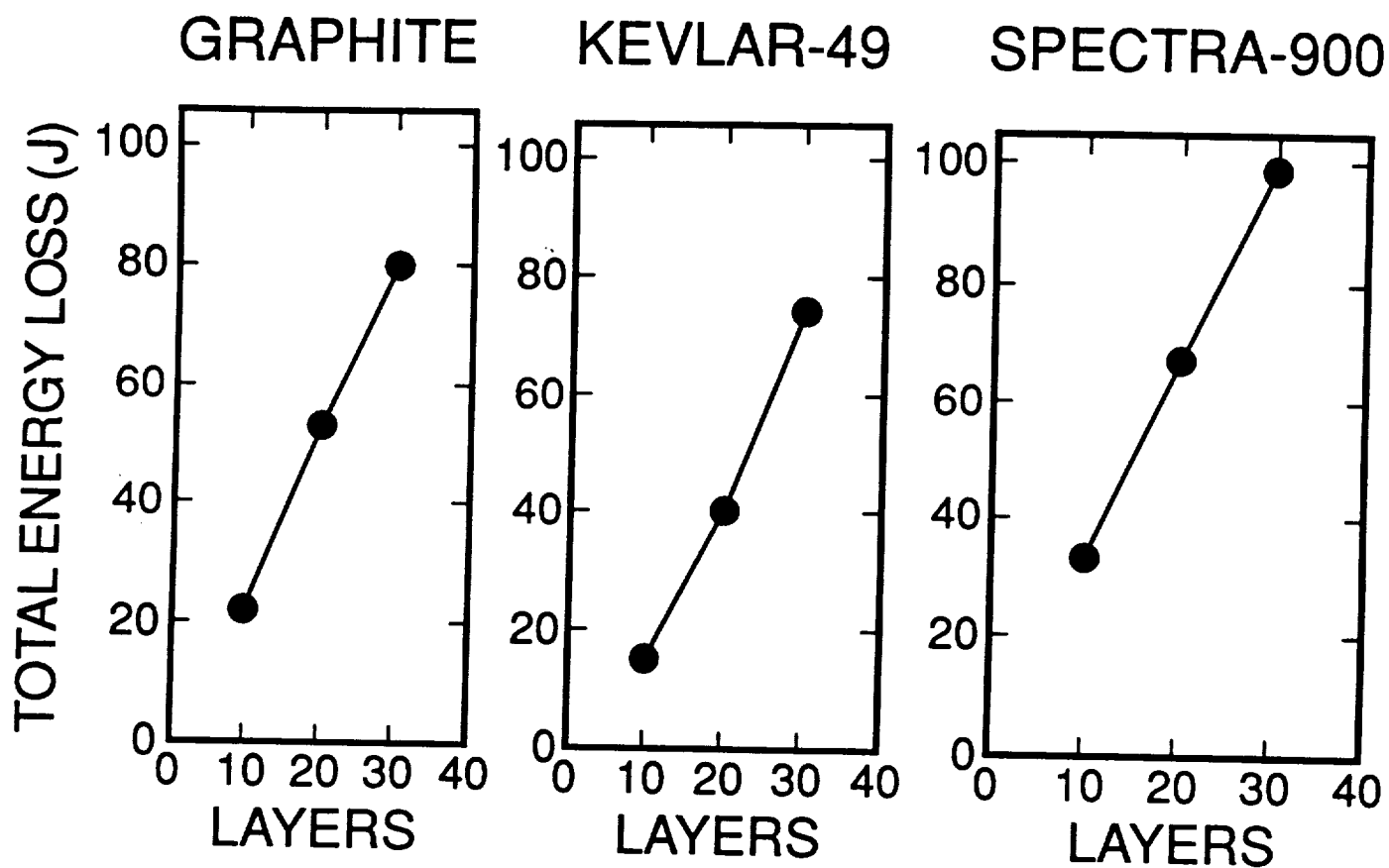


Figure 46. Total energy loss for PE, Kevlar-49 and graphite reinforced composites as a function of number of layers when impacted by a high velocity projectile.

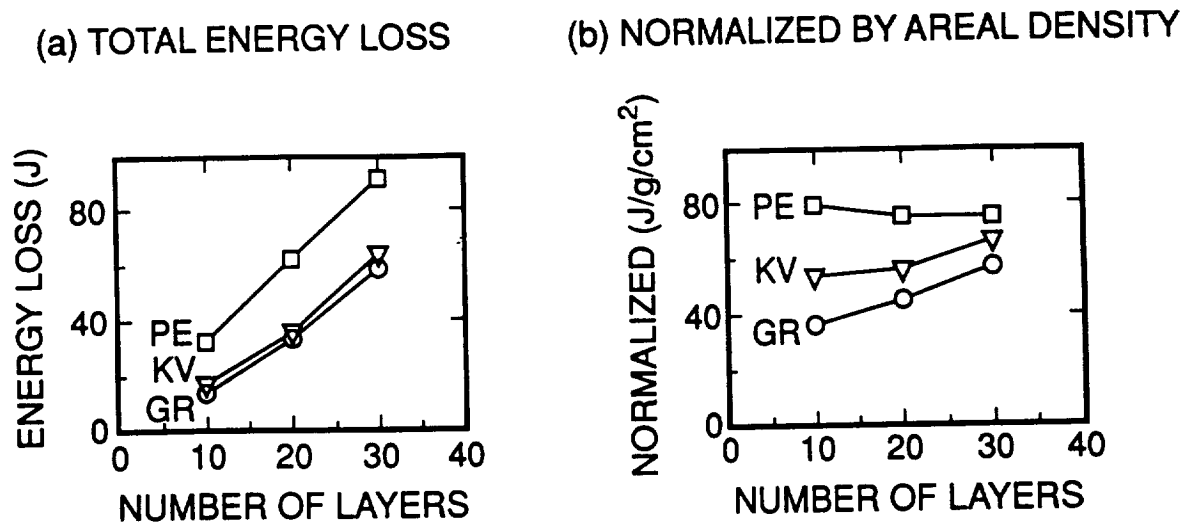


Figure 47. Energy absorption characteristics of the three types of fiber reinforced composites as a function of (a) number of layers and (b) normalized to the areal density.

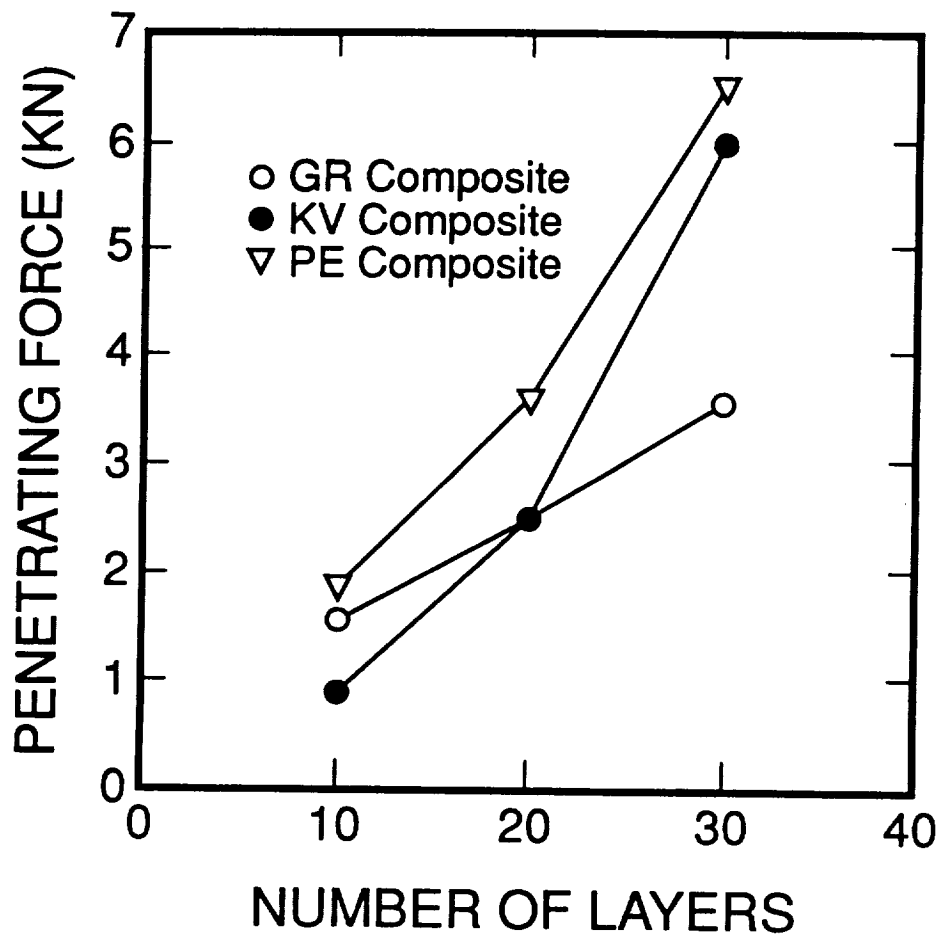


Figure 48. The average force of penetration calculated from the slope of the energy loss curves for Spectra-900 PE, Kevlar-49 and graphite composites.

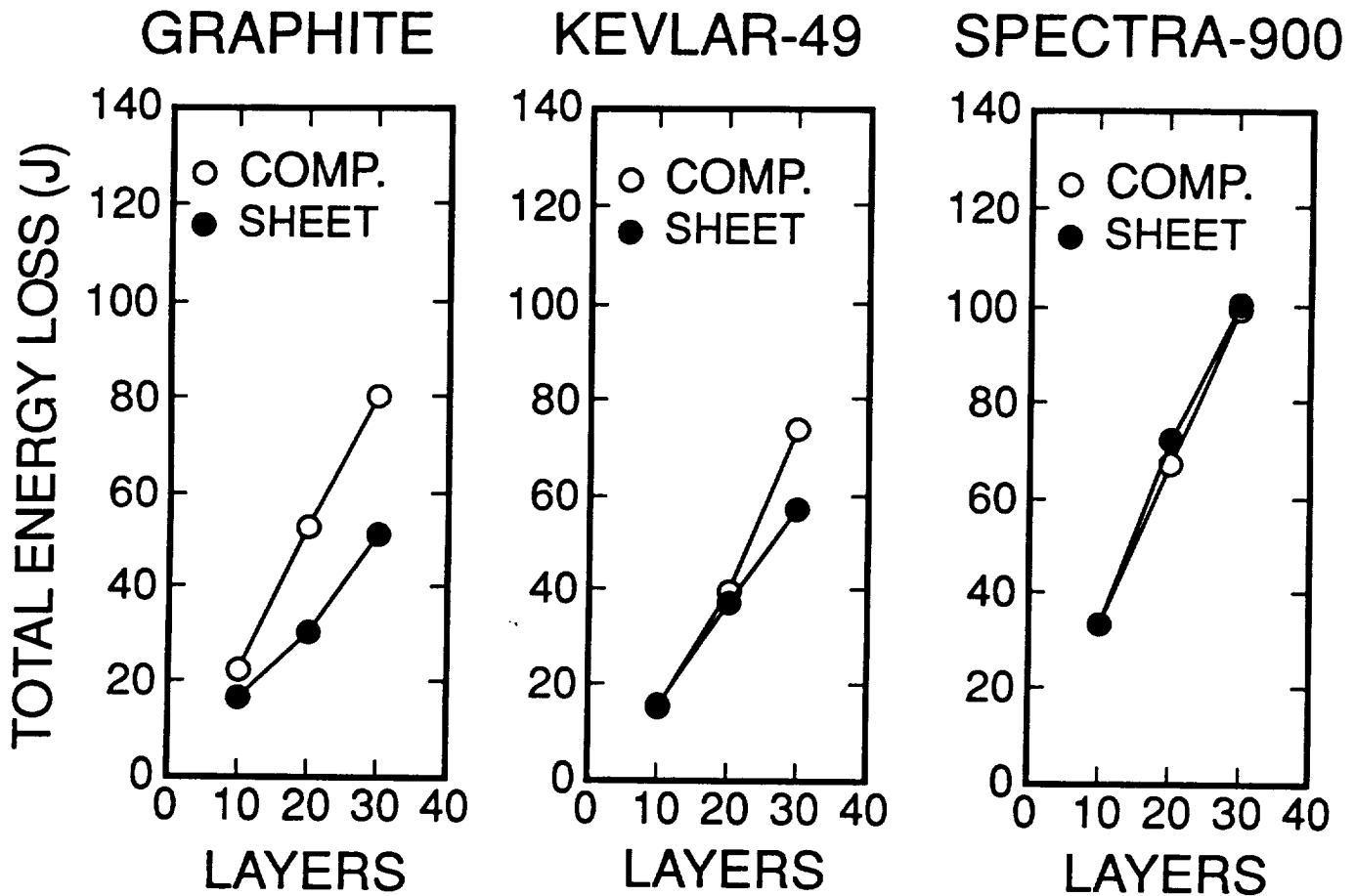


Figure 49. A comparison of the total energy loss between the composites and the stacked sheets configuration illustrating the contribution from delamination.

